Characterization of oxide-based catalysts and model catalysts for renewable fuels

Gericke, Sabrina Maria

2024

Characterization of oxide-based catalysts and model catalysts for renewable fuels

SABRINA M. GERICKE
DEPARTMENT OF PHYSICS | FACULTY OF ENGINEERING | LUND UNIVERSITY
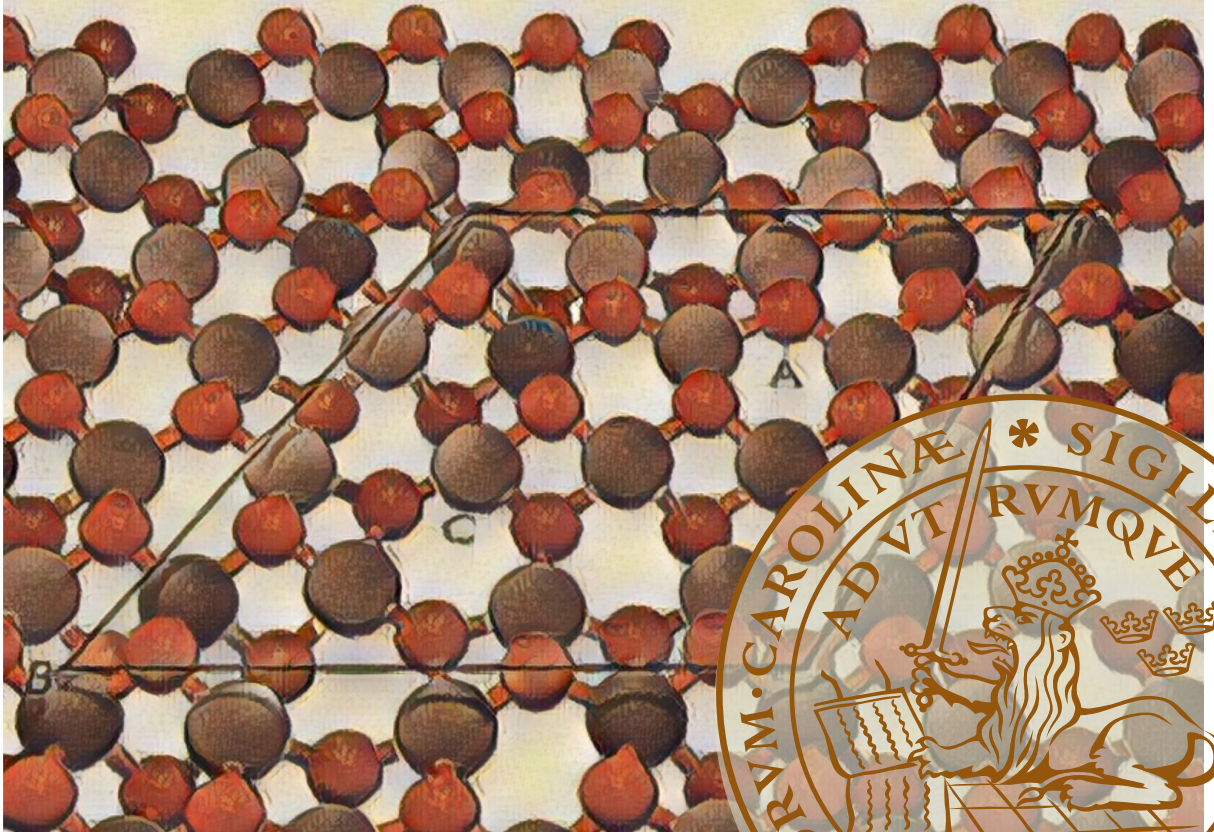
Characterization of oxide-based catalysts and model catalysts for renewable fuels

Characterization of oxide-based catalysts and model catalysts for renewable fuels

by Sabrina M. Gericke

LUND
UNIVERSITY

Thesis for the degree of Doctor of Philosophy
Thesis advisors: Doc. Johan Zetterberg, Prof. Edvin Lundgren, Doc. Hampus Nilsson
and Dr. Sara Blomberg
Faculty opponent: Prof. Zdenek Dohnalek

To be presented, with the permission of the Faculty of Engineering at Lund University, for public criticism in
the Rydberg hall at the Department of Physics on Friday, the 5th of April 2024 at 09:15.

Organization **LUND UNIVERSITY**	Document name **DOCTORAL DISSERTATION**	
Department of Physics Box 118 SE–221 00 Lund Sweden	Date of disputation 2024-04-05	
	Sponsoring organization	

Author(s)
Sabrina M. Gericke

Title and subtitle
Characterization of oxide-based catalysts and model catalysts for renewable fuels

Abstract

This thesis presents fundamental studies on oxide-based catalysts and model catalysts used for the synthesis of renewable fuels. The two investigated oxide catalysts are $In_2O_3(111)$ model catalysts and NiMo-oxide catalysts.

The $In_2O_3(111)$ surface is studied as a model system for In_2O_3-based catalysts used for CO_2 hydrogenation to methanol. Specifically, the interaction of $In_2O_3(111)$ with CO_2, syngas and potential reaction intermediates were investigated using photoelectron spectroscopy and complementary DFT calculations. These investigations provide insights in the adsorption geometry of the respective molecules on the surface. Additionally, the poising effect of H_2O and H_2S on the CO_2 adsorption on the $In_2O_3(111)$ was investigated, showing how dissociated H_2O limits the CO_2 adsorption and how dissociated H_2S blocks CO_2 adsorption on the $In_2O_3(111)$ surface.

The second part of this thesis investigates the reduction of NiMo-oxide catalysts on alumina support and compares it to the reduction behavior of different model systems for these catalysts. The *in situ* studies show that Ni and Mo facilitate each others reduction and highlight the impact of the alumina support and noble metal promotors on the reduction of the NiMo-oxide catalysts. To gain a detailed insight into the reduction process of NiMo-oxide catalysts, we designed a model system of these catalysts based on $NiMoO_4$ nanoparticles and studied their reduction, which proceeds through a phase separation of Ni- and Mo-oxide.

Key words
In_2O_3, NiMo-oxide, reduction, CO_2 adsorption, model catalysis, photoelectron spectroscopy, oxide catalysts, CO_2 hydrogenation

Classification system and/or index terms (if any)

Supplementary bibliographical information	Language English
ISSN and key title	ISBN 978-91-8039-988-3 (print) 978-91-8039-989-0 (pdf)

Recipient's notes	Number of pages 162	Price
	Security classification	

Signature _____   Date ___2024-02-21___

Characterization of oxide-based catalysts and model catalysts for renewable fuels

by Sabrina M. Gericke

Cover illustration front: Illustration of the oxide catalysts studied in this thesis, showing a $NiMoO_x$/ Al_2O_3 catalyst on the top left, $NiMoO_4$ nanoparticles on the top right and the $In_2O_3(111)$ surface on the bottom.

Cover illustration back: *In situ* DRIFTS measurements of pyridine desorption from a $NiMo/Al_2O_3$ catalyst.

Faculty of Engineering, Department of Physics

Dedicated to everyone who helped me along the way.

Contents

List of publications

This thesis is based on the following publications, referred to by their Roman numerals.

I. Gericke, S. M., Kauppinen, M. M., Wagner, M., Riva, M., Franceschi, G., Posada-Borbón, A., Rämisch, L., Pfaff, S., Rheinfrank, E., Imre, A. M., Preobrajenski, A. B., Appelfeller, S., Blomberg, S., Merte, L. R., Zetterberg, J., Diebold, U., Grönbeck, H. & Lundgren, E. **Effect of Different In$_2$O$_3$(111) Surface Terminations on CO$_2$ Adsorption**. *ACS Applied Materials and Interfaces* **15,** 45367–45377 (2023).

II. Gericke, S. M., Kauppinen, M. M., Wagner, M., Riva, M., Franceschi, G., Rämisch, L., Pfaff, S., Ryan, P., Rheinfrank, E., Imre, A. M., Blomberg, S., Scardamaglia, M., Wang, W., Zetterberg, J., Diebold, U., Grönbeck, H. & Lundgren, E. **Interaction of In$_2$O$_3$(111) with syngas and the effect of sulfur contaminant on CO$_2$ adsorption on In$_2$O$_3$(111)**. *Manuscript.*

III. Gericke, S. M., Rissler, J., Bermeo, M., Wallander, H., Karlsson, H., Kollberg, L., Scardamaglia, M., Temperton, R., Zhu, S., Sigfridsson Clauss, K. G., Hulteberg, C., Shavorskiy, A., Merte, L. R., Messing, M. E., Zetterberg, J. & Blomberg, S. **In Situ H$_2$ Reduction of Al$_2$O$_3$-Supported Ni- and Mo-Based Catalysts**. *Catalysts* **12,** 548–553 (2022).

IV. Elmroth Nordlander, J., Gericke, S. M., Bermeo Vargas, M., Ternero, P., Wahlqvist, D., Hallböök, F., Scardamaglia, M., Zetterberg, J., Ek, M., Messing, M. & Blomberg, S. **In situ AP-XPS reduction study of engineered NiMoO$_4$ nanoparticles**. *Manuscript.*

V. Hallböök, F., Gericke, S. M., Kristensen, T., Elmroth Nordlander, J., Karagoz, B., Van Spronsen, M., Hulteberg, C., Zetterberg, J. & Blomberg, S. **In situ APXPS and TPR reduction study of Pd-NiMo and Ru-NiMo catalysts**. *Manuscript.*

Related Work

The following papers are related work but not included in the thesis.

A. Rämisch, L., Pfaff, S., Gericke, S. M., Lundgren, E. & Zetterberg, J. **Ambient pressure operando catalytic characterization by combining PM-IRRAS with planar laser-induced fluorescence and surface optical reflectance imaging**. *Catalysis Today* **427,** 114441 (2024).

B. Hu, T., Gericke, S. M., Tong, X., Nykypanchuk, D., Kristensen, T., Hulteberg, C., Stacchiola, D., Blomberg, S. & Head, A. R. **Interaction of Anisole on Alumina-Supported Ni and Mo Oxide Hydrodeoxygenation Catalysts**. *Journal of Physical Chemistry C* **127,** 19440–19450 (2023).

C. Pfaff, S., Larsson, A., Orlov, D., Rämisch, L., Gericke, S. M., Lundgren, E. & Zetterberg, J. **A Polycrystalline Pd Surface Studied by Two-Dimensional Surface Optical Reflectance during CO Oxidation: Bridging the Materials Gap**. *ACS Applied Materials Interfaces* **16,** 244701 (2023).

D. Koller, V., Lustemberg, P. G., Spriewald-Luciano, A., Gericke, S. M., Larsson, A., Sack, C., Preobrajenski, A., Lundgren, E., Ganduglia-Pirovano, M. V. & Over, H. **Critical Step in the HCl Oxidation Reaction over Single-Crystalline $CeO_{2-x}(111)$: Peroxo-Induced Site Change of Strongly Adsorbed Surface Chlorine**. *ACS Catalysis* **13,** 12994–13007 (2023).

E. Degerman, D., Shipilin, M., Lömker, P., Goodwin, C. M., Gericke, S. M., Hejral, U., Gladh, J., Wang, H. Y., Schlueter, C., Nilsson, A. & Amann, P. **Operando Observation of Oxygenated Intermediates during CO Hydrogenation on Rh Single Crystals**. *Journal of the American Chemical Society* **144,** 7038–7042 (2022).

F. Pfaff, S., Rämisch, L., Gericke, S. M., Larsson, A., Lundgren, E. & Zetterberg, J. **Visualizing the Gas Diffusion Induced Ignition of a Catalytic Reaction**. *ACS Catalysis* **12,** 6589–6595 (2022).

G. Rämisch, L., Gericke, S. M., Pfaff, S., Lundgren, E. & Zetterberg, J. **Infrared surface spectroscopy and surface optical reflectance for operando catalyst surface characterization**. *Applied Surface Science* **578,** 152048 (2022).

H. Temperton, R. H., Kawde, A., Eriksson, A., Wang, W., Kokkonen, E., Jones, R., Gericke, S. M., Zhu, S., Quevedo, W., Seidel, R., Schnadt, J., Shavorskiy, A., Persson, P. & Uhlig, J. **Dip-and-pull ambient pressure photoelectron spectroscopy as a spectroelectrochemistry tool for probing molecular redox processes**. *Journal of Chemical Physics* **157,** 244701 (2022).

I. Garcia-Martinez, F., Dietze, E., Schiller, F., Gajdek, D., Merte, L. R., Gericke, S. M., Zetterberg, J., Albertin, S., Lundgren, E., Grönbeck, H. & Ortega, J. E. **Reduced Carbon Monoxide Saturation Coverage on Vicinal Palladium Surfaces: The Importance of the Adsorption Site**. *Journal of Physical Chemistry Letters* **12,** 9508–9515 (2021).

J. Pfaff, S., Larsson, A., Orlov, D., Harlow, G. S., Abbondanza, G., Linpé, W., Rämisch, L., Gericke, S. M., Zetterberg, J. & Lundgren, E. **Operando Reflectance Microscopy on Polycrystalline Surfaces in Thermal Catalysis, Electrocatalysis, and Corrosion**. *ACS Applied Materials and Interfaces* **13,** 19530–19540 (2021).

K. Baeumer, C., Li, J., Lu, Q., Liang, A. Y. L., Jin, L., Martins, H. P., Duchoň, T., Glöß, M., Gericke, S. M., Wohlgemuth, M. A., Giesen, M., Penn, E. E., Dittmann, R., Gunkel, F., Waser, R., Bajdich, M., Nemšák, S., Mefford, J. T. & Chueh, W. C. **Tuning electrochemically driven surface transformation in atomically flat LaNiO$_3$ thin films for enhanced water electrolysis**. *Nature Materials* **20,** 674–682 (2021).

L. Abb, M. J. S., Weber, T., Langsdorf, D., Koller, V., Gericke, S. M., Pfaff, S., Busch, M., Zetterberg, J., Preobrajenski, A., Grönbeck, H., Lundgren, E. & Over, H. **Thermal Stability of Single-Crystalline IrO$_2$(110) Layers: Spectroscopic and Adsorption Studies**. *Journal of Physical Chemistry C* **124,** 15324–15336 (2020).

M. Gericke, S. M., Mulhearn, W. D., Goodacre, D. E., Raso, J., Miller, D. J., Carver, L., Nemšák, S., Karslloglu, O., Trotochaud, L., Bluhm, H., Stafford, C. M. & Buechner, C. **Water-polyamide chemical interplay in desalination membranes explored by ambient pressure X-ray photoelectron spectroscopy**. *Physical Chemistry Chemical Physics* **22,** 15658–15663 (2020).

N. Goodacre, D., Blum, M., Buechner, C., Hoek, H., Gericke, S. M., Söhnel, T., Bluhm, H., Franklin, J. B., Kittiwatanakul, S. & Kevin, E. **Water adsorption on vanadium oxide thin films in ambient relative humidity Water adsorption on vanadium oxide thin films in ambient relative humidity**. *The Journal of Chemical Physics* **152,** 044715 (2020).

O. Buechner, C., Gericke, S. M., Trotochaud, L., Karslloglu, O., Raso, J. & Bluhm, H. **Quantitative Characterization of a Desalination Membrane Model System by X-ray Photoelectron Spectroscopy**. *Langmuir* **35,** 11315–11321 (2019).

Abstract

This thesis presents fundamental studies on oxide-based catalysts and model catalysts used for the synthesis of renewable fuels. The two investigated oxide catalysts are $In_2O_3(111)$ model catalysts and NiMo-oxide catalysts.

The $In_2O_3(111)$ surface is studied as a model system for In_2O_3-based catalysts used for CO_2 hydrogenation to methanol. Specifically, the interaction of $In_2O_3(111)$ with CO_2, syngas and potential reaction intermediates were investigated using photoelectron spectroscopy and complementary DFT calculations. These investigations provide insights in the adsorption geometry of the respective molecules on the surface. Additionally, the poising effect of H_2O and H_2S on the CO_2 adsorption on the $In_2O_3(111)$ was investigated, showing how dissociated H_2O limits the CO_2 adsorption and how dissociated H_2S blocks CO_2 adsorption on the $In_2O_3(111)$ surface.

The second part of this thesis investigates the reduction of NiMo-oxide catalysts on alumina support and compares it to the reduction behavior of different model systems for these catalysts. The *in situ* studies show that Ni and Mo facilitate each others reduction and highlight the impact of the alumina support and noble metal promotors on the reduction of the NiMo-oxide catalysts. To gain a detailed insight into the reduction process of NiMo-oxide catalysts, we designed a model system of these catalysts based on $NiMoO_4$ nanoparticles and studied their reduction, which proceeds through a phase separation of Ni- and Mo-oxide.

Popular Summary in English

The possibly devastating consequences of global warming have gained increasing attention in recent years. Increasing efforts are made to decrease the emission of greenhouse gases to the atmosphere in an attempt to avert climate change. The goal is to transform our energy economy, which is currently predominantly running on fossil fuels into a sustainable energy economy relying on renewable energy sources. One of the pillars of such a sustainable energy economy are renewable fuels that can be produced from biomass or the CO_2 hydrogenation with H_2 from solar driven water splitting.

The upcycling of biomass or CO_2 to renewable fuels are complex chemical processes that typically require an additional substance, called a catalyst. A catalyst is a substance that is added to a chemical reaction in order to modify the pathway of the chemical reaction. The catalyst can be used to reduce the energy that is required for the reaction by reducing the reaction temperature or the required pressure. Additionally, the catalyst can steer the reaction along a specific reaction pathway to increase the production of a certain reaction product and, thus, reduce the production of undesired waste products. The catalyst takes part in the reaction and returns to its original state afterwards so it can take part in another reaction cycle and is not consumed by the reaction.

Today's catalysts suffer from a range of problems. Many catalysts rely on precious metals which are expensive and may not be available in sufficient quantity. Additionally, the lifetime of a catalyst is limited by a range of deactivation processes. To overcome these and other limitations of current catalysts, researchers and engineers strive to improve the design of catalysts. The development of these future catalysts benefits from a detailed understanding of how catalysts work - meaning how reactants interact with the catalyst, how the composition of the catalyst influences its behavior and what processes cause the deactivation of catalysts.

The work presented in this thesis tries to answer a few of these fundamental questions for two catalytical systems used for the synthesis of renewable fuels. The two systems that were studied are In_2O_3 model catalysts for CO_2 hydrogenation to methanol and $NiMo/Al_2O_3$ catalysts for the upcycling of plant-based waste products to biofuels. For the In_2O_3 model catalysts the interaction of the reactant gas CO_2 was studied in detail to understand where on the catalyst's surface the CO_2 adsorbs and how its adsorption is blocked by possible contaminants. The investigations on the $NiMo/Al_2O_3$ catalysts focus on how the composition and additional noble metal promotion of the catalysts influences the reduction of these catalysts.

Populärvetenskaplig sammanfattning på svenska

De potentiellt förödande konsekvenserna av den globala uppvärmningen har fått allt större uppmärksamhet under de senaste åren. Allt större ansträngningar görs för att minska utsläppen av växthusgaser i atmosfären i syfte att minimera effekterna av klimatförändringarna. Målet är att omvandla vår energiekonomi, som för närvarande huvudsakligen baseras på fossila bränslen, till en hållbar energiekonomi baserad på förnybara energikällor. En av grundpelarna i en sådan hållbar energiekonomi är förnybara bränslen, som kan framställas av biomassa eller genom hydrogenering av CO_2 med H_2 från soldriven vattenklyvning.

Omvandlingen av biomassa eller CO_2 till förnybara bränslen är en komplex kemisk process som vanligtvis kräver en ytterligare substans, en så kallad katalysator. En katalysator är en substans som tillsätts till en kemisk reaktion för att styra reaktionen. Katalysatorn kan användas för att minska den energi som krävs för reaktionen genom att sänka reaktionstemperaturen eller reaktionstrycket. Katalysatorn kan också styra reaktionen i en viss riktning för att öka produktionen av en viss reaktionsprodukt och därmed minimera produktionen av oönskade avfallsprodukter. Katalysatorn deltar i reaktionen och återgår sedan till sitt ursprungliga tillstånd så att den kan delta i en annan reaktionscykel och inte förbrukas av reaktionen.

Dagens katalysatorer har ett antal problem. Många katalysatorer är beroende av ädelmetaller, som är dyra och som kanske inte finns tillgängliga i tillräckliga mängder. Dessutom begränsas katalysatorns livslängd av ett antal deaktiveringsprocesser. För att övervinna dessa och andra begränsningar hos dagens katalysatorer strävar forskare och ingenjörer efter att förbättra utformningen av katalysatorer. Utvecklingen av dessa framtida katalysatorer gynnas av en detaljerad förståelse av hur katalysatorer fungerar. Forskarna försöker förstå hur reaktanter interagerar med katalysatorer, hur katalysatorers sammansättning påverkar dess beteende och vilka processer som orsakar deaktivering av katalysatorer.

Denna avhandling försöker besvara några av dessa grundläggande frågor för två katalytiska system som används för syntes av förnybara bränslen. De två system som undersökts är In_2O_3-modellkatalysatorer för CO_2 hydrogenering till metanol och $NiMo/Al_2O_3$-katalysatorer för upcycling av växtavfallsprodukter till biobränslen. För In_2O_3-modellkatalysatorer undersöktes interaktionen med reaktionsgasen CO_2 i detalj för att förstå var på katalysatorytan CO_2 adsorberas och hur dess adsorption kan blockeras av eventuella föroreningar. Undersökningarna av $NiMo/Al_2O_3$-katalysatorerna fokuserar på hur sammansättningen och tillsättning av ädelmetaller till katalysatorerna påverkar reduktionen av dessa katalysatorer.

Populärwissenschaftliche Zusammenfassung auf Deutsch

Die möglicherweise verheerenden Folgen der globalen Erwärmung haben in den letzten Jahren zunehmend an Aufmerksamkeit gewonnen. Wachsende Anstrengungen werden unternommen, um die Emission von Treibhausgasen in die Atmosphäre zu verringern und so die Auswirkungen des Klimawandels zu minimieren. Ziel ist es, unsere Energiewirtschaft, die derzeit überwiegend auf fossilen Brennstoffen basiert, in eine nachhaltige Energiewirtschaft umzuwandeln, die sich auf erneuerbare Energiequellen stützt. Eine der Säulen einer solchen nachhaltigen Energiewirtschaft sind erneuerbare Kraftstoffe, die aus Biomasse oder der Hydrierung von CO_2 mit H_2 aus solarbetriebener Wasserspaltung gewonnen werden können.

Die Umwandlung von Biomasse oder CO_2 in erneuerbare Kraftstoffe ist ein komplexer chemischer Prozess, der in der Regel einen zusätzlichen Stoff, einen so genannten Katalysator, erfordert. Ein Katalysator ist eine Substanz, die einer chemischen Reaktion hinzugefügt wird, um die Reaktion zu steuern. Der Katalysator kann dazu dienen, die für die Reaktion erforderliche Energie zu reduzieren, indem er die Reaktionstemperatur oder den erforderlichen Druck senkt. Außerdem kann der Katalysator die Reaktion in eine bestimmte Richtung lenken, um die Produktion eines bestimmten Reaktionsprodukts zu erhöhen und damit die Produktion unerwünschter Abfallprodukte zu minimieren. Der Katalysator nimmt an der Reaktion teil und kehrt danach in seinen ursprünglichen Zustand zurück, so dass er an einem weiteren Reaktionszyklus teilnehmen kann und nicht durch die Reaktion verbraucht wird.

Die heutigen Katalysatoren sind mit einer Reihe von Problemen behaftet. Viele Katalysatoren sind auf Edelmetalle angewiesen, die teuer sind und möglicherweise nicht in ausreichender Menge zur Verfügung stehen. Außerdem ist die Lebensdauer eines Katalysators durch eine Reihe von Deaktivierungsprozessen begrenzt. Um diese und andere Einschränkungen der derzeitigen Katalysatoren zu überwinden, bemühen sich Forscher und Ingenieure um eine Verbesserung des Designs von Katalysatoren. Die Entwicklung dieser zukünftigen Katalysatoren profitiert von einem detaillierten Verständnis der Funktionsweise von Katalysatoren. Forscher versuchen zu verstehen wie die Reaktanten mit dem Katalysator interagieren, wie die Zusammensetzung des Katalysators sein Verhalten beeinflusst und welche Prozesse die Deaktivierung von Katalysatoren verursachen.

Dieser Doktorarbeit trägt dazu bei, einige dieser grundlegenden Fragen für zwei katalytische Systeme zu beantworten, die für die Synthese von erneuerbaren Kraftstoffen verwendet werden. Bei den beiden untersuchten Systemen handelt es sich um In_2O_3-Modellkatalysatoren für die CO_2-Hydrierung zu Methanol und $NiMo/Al_2O_3$-Katalysatoren für das Upcycling von pflanzlichen Abfallprodukten zu Biokraftstoffen. Für die In_2O_3-Modellkatalysatoren wurde die Wechselwirkung mit dem Reaktionsgas CO_2 untersucht, um zu verste-

hen, wo auf der Katalysatoroberfläche das CO_2 adsorbiert und wie seine Adsorption durch mögliche Verunreinigungen blockiert werden kann. Die Untersuchungen der NiMo/Al$_2$O$_3$-Katalysatoren konzentrieren sich darauf, wie die Zusammensetzung und der Einsatz von edelmetallhaltigen Promotoren die Reduktion dieser Materialien beeinflussen.

Acknowledgements

Abbreviations

APXPS	Ambient Pressure X-ray Photoelectron Spectroscopy
CLS	Core Level Shift
cus	coordinatively unsaturated
DFT	Density Functional Theory
DRIFTS	Diffuse Reflectance Infrared Fourier Transform Spectroscopy
E_{act}	activation energy
E_{bin}	binding energy
E_{kin}	kinetic energy
EBSD	Electron Backscatter Diffraction
EPU	Elliptically Polarizing Undulator
HDO	Hydrodeoxygenation
LEED	Low Energy Electron Diffraction
PMG	Plane Grating Monochromator
RWGS	Reverse Water Gas Shift
STEM	Scanning Transmission Electron Microscopy
STM	Scanning Tunneling Microscopy
TEM	Transmission Electron Microscopy
TPR	Temperature Programmed Reduction
UHV	Ultra High Vacuum
XANES	X-ray Absorption Near Edge Structure
XAS	X-ray Absorption Spectroscopy
XPS	X-ray Photoelectron Spectroscopy
XRD	X-Ray Diffraction
YSZ	Yttria-Stabilized Zirconia

Chapter 1

Introduction

The chemical industry is one of the pillars of our modern society. From fertilizer to poly-mers, over pharmaceutics, plastics and paints - most of the goods produced today require a catalyst somewhere in their production chain [1]. So, what is a catalyst and why is it so crucial to the chemical industry? In general terms, a catalyst is a substance that facilitates a chemical reaction but is not consumed by the reaction.

The research field catalysis is divided into two areas - homogenoeus catalysis and hetero-geneous catalysis. In homogenoeus catalysis the catalyst and the reactants are in the same phase, most often in the liquid phase. In heterogeneous catalysis, on the other hand, the catalyst and the reactants are in different phases. Typically, the catalyst is a solid and the reactants are in gas or liquid phase.

The first use of an inorganic catalyst is attributed to Valerius Cordus in 1552, when he used sulfuric acid to catalyze the conversion of alcohol to ether [2]. The term 'catalyst' was established nearly 300 years later by Jöns Jacob Berzelius [3]. Since the establishment of the research field, the catalytic properties of materials have been investigated intensively. Wilhelm Ostwald, Paul Sabatier and Fritz Haber were awarded the Nobel price in chemistry in 1909, 1912 and 1918, respectively, for their work on different catalytic processes [2].

In heterogeneous catalysis, catalysts are often rare metals or rare metal oxides. Since these are expensive materials, efforts are made to reduce the costs of the catalyst by maximizing its surface area, in order to have as many active sites per gram of catalyst as possible. This is typically done by depositing nanoparticles of the catalytic material onto a support material. These supported nanoparticles are then used to catalyze reactions at pressures up to several hundreds bar and temperatures of several hundreds °C.

While most of the early scientific work on catalysis was conducted using a trial-and-error

approach to find the best catalyst and the best reaction conditions, there was also a drive towards a more fundamental understanding of catalytic processes. To gain a detailed understanding of the reaction mechanisms on surfaces, surface scientists investigated model surfaces of catalytic materials under well-controlled conditions (often at very low pressures and temperatures). The samples used in these studies are often single crystalline surfaces that model individual facets of the catalytic nanoparticles. Over the years, surface scientists have gained detailed knowledge about the interaction of reactants with surfaces and in 2007 Gerhard Ertl was awarded the Nobel Price in Chemistry for his contributions to the field of catalysis through his work in the field of surface science [4].

However, the question remains to what extent the results obtained under the highly controlled conditions of surface science studies are also applicable to the less controlled environment of industrial catalytic reactions. Two fundamental gaps have been identified between the surface science approach and industrial catalysis: the materials gap and the pressure gap. In recent years the surface science community is striving increasingly towards bridging these gaps. To investigate the effect of the materials gap, increasingly complex model systems studied such as polycrystalline sample and size controlled nanoparticles. At the same time, instrumental developments allow to extend the pressure range at which surface science experiments can be performed, slowly bridging the pressure gap.

This thesis investigates the effect of the materials gap on one catalytic system and the effect of the pressure gap on another catalytic system. The catalysts that were studied, are an $In_2O_3(111)$ model catalyst and alumina supported NiMo-oxide catalysts. $In_2O_3(111)$ was used as a model system for In_2O_3-based catalysts for the hydrogenation of CO_2 to methanol. Paper [I] is a fundamental surface science study addressing the adsorption of CO_2 on different surface terminations of $In_2O_3(111)$. The second manuscript on $In_2O_3(111)$ [II] investigates how the surface behaves under elevated pressure and temperature and studies the poisoning effect of sulfur. The investigations on the NiMo-oxide catalysts focus on the reduction of these catalysts. In the first NiMo paper [III], we studied the effect of the materials gap on the reduction of NiMo-oxide catalysts. In the second NiMo paper [IV], we investigate how $NiMoO_4$-nanoparticles reduce under the same conditions as in paper [III], which provides deeper insight into the effect of the materials gap for these NiMo-systems. In the final manuscript [V], we turn our attention back on the Al_2O_3-supported NiMo-oxide catalysts and study how the promotion with Ruthenium (Ru) and Palladium (Pd) influences the reduction of these catalysts.

Chapter 2

Crystals and Surface Science

The catalysts used in heterogeneous catalysis are often crystalline metals or metal oxides, and their crystalline and surface structure have a significant impact on their catalytic performance. This chapter gives an overview on the surface and crystalline structure of the materials studied in this thesis. The chapter begins with a brief introduction to crystal structures. The following sections introduce surfaces of crystals and how gases adsorb on these surfaces, as well as how gas adsorbtion can be blocked if surfaces are poisoned by other adsorbates. Finally, the last section gives an overview on the structure of the two catalytic materials studied in this thesis In_2O_3 and Ni- and Mo-based oxides.

2.1 Crystals

Many solid materials form crystals. A crystal is a solid in which the atoms are arranged in a periodical manner consisting of repeating units. In order to describe a crystalline structure one needs to know what the smallest repeating unit looks like and how these repeating units are arranged relative to each other. The smallest repeating unit within a crystal is called the unit cell. A unit cell can enclose just a single atom or it can be made of multiple atoms. Typically, the unit cells of metals contain just a few atoms while the unit cells of alloys and oxides can be more complex.

There are in total 14 different crystal lattice structures that describe the periodic arrangement of unit cells within a crystal. These 14 lattice structures are referred to Bravais Lattice, named after Auguste Bravais who conceived this set of structures in 1850 [5]. The lattices are characterized by the relative dimensions and angles of their corresponding unit cells. Since this thesis only discusses materials with certain structures, we limit the discussion on crystal structures to these five structures.

(a)   simple cubic   (c)   rhombohedral   (d)   monoclinic

$\vec{a_3}$

$\vec{a_2}$

$\vec{a_1}$

$a_1 = a_2 = a_3$
$\alpha = \beta = \gamma = 90°$

$a_1 = a_2 = a_3$
$\alpha = \beta = \gamma \neq 90°$

$a_1 \neq a_2 \neq a_3$
$\alpha = \gamma = 90°$
$\beta \neq 90°$

(b)   orthorhombic   (e)   hexagonal

$a_1 \neq a_2 \neq a_3$
$\alpha = \beta = \gamma = 90°$

$a_1 = a_2 \neq a_3$
$\alpha = \beta = 90°, \gamma = 120°$
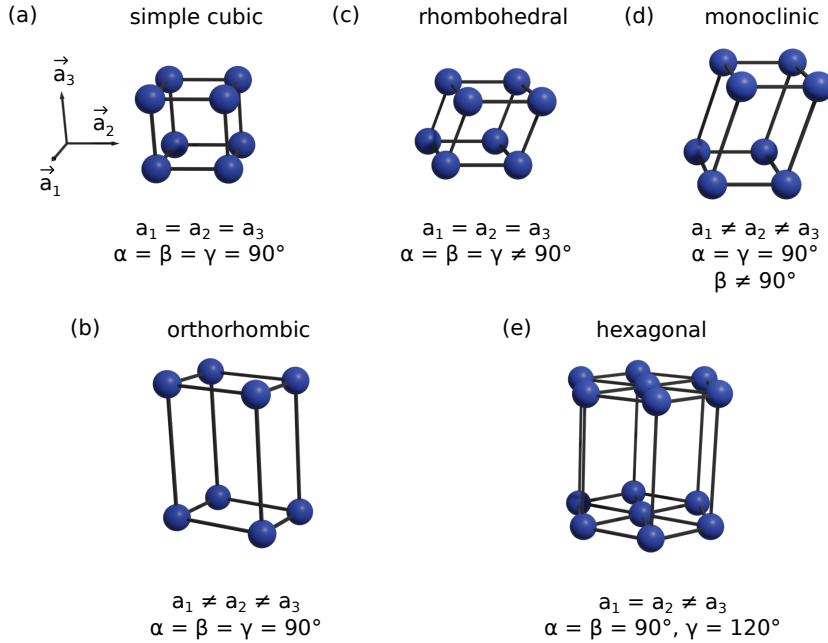
Figure 2.1: Illustrations of the 3D Bravais Lattice of materials discussed in this thesis showing (a) a simple cubic structure, (b) an orthorhombic structure, (c) a rhombohedral structure, (d) a monoclinic structure and (e) a hexagonal structure.

The simplest crystal structure is the simple cubic structure, which is displayed in Figure 2.1(a). All edges of the unit cell are the same length and all angles within the unit cell are 90° making the unit cell a cube. In the simple cubic structure one atom is placed at each of the corners of the unit cell, thus, each atom has 6 nearest neighbours at equal distance.

Figure 2.1(b) shows a orthorhombic unit cell in which all angles are 90° but all edges have different lengths. Figure 2.1(c) displays a rhombohedral unit cell. In this crystal structure, all edges of the unit cell are equally long and all angles are equal, but in contrast to the cubic structure all angles are unequal 90°. Figure 2.1(d) shows a monoclinic unit cell with three unequally long edges. Two of the angles in this cell are equal to 90°, while the third angle is unequal 90°. Finally, Figure 2.1(e) shows a hexagonal structure.

2.2   Surface structure

In addition to the crystalline structure of the bulk, a crystal also has a surface. The structure of this surface differs from the bulk structure due to the lack of atoms in one direction on the
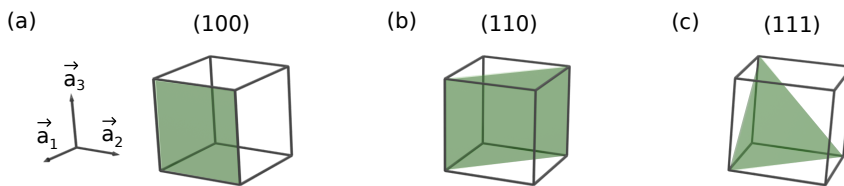
Figure 2.2: Illustration of the (100), (110) and (111) plane in a simple cubic unit cell. The orientation of the respective planes is marked in green.

surface. The surface structure is of particular interest for the research field of catalysis since the catalytic reactions take place on the surface. The properties of surfaces are dependent on how the bulk crystal is cut to obtain the surface.

The different orientations within a crystal are differentiated by the so-called Miller indices *h*, *k* and *l*. These Miller indices can be used in different notations to denote either a lattice plane as (*hkl*), or a set of equivalent lattice planes {*hkl*}, a direction in the basis of the lattice vectors orthogonal to the surface [*hkl*] or a set of equivalent directions as <*hkl*>.

In the field of surface science, Miller indices are used to denote the lattice plane along which a crystal is cut to obtain a particular surface as (*hkl*). The indices h,k and l give the points of intersection of the described crystal plane with the lattice vectors $\vec{a_1}$, $\vec{a_2}$ and $\vec{a_3}$, respectively. As an example Figure 2.2 illustrates how to cut a simple cubic unit cell to obtain a low index surface with the (100), (110) or (111) orientation.

The surface orientation of a crystal is of high importance for its catalytic properties. Since the surface properties have a crucial effect on the chemical reactions on the surface and can steer the selectivity and activity of the catalyst. For example, it has been shown that Cu(100) is a good electrochemical catalyst for C_2H_4 synthesis, while it shows very low selectivity for CH_4. On the other hand, the opposite is observed for the Cu(111) surface [6].

2.3 Adsorption sites and poisoning

When a gas molecule adsorbs on a surface, it can do so in different ways. Depending on the structure of the surface, it may adsorb coordinating to a single atom, or coordinating to multiple atoms. Figure 2.3 illustrates the different adsorption sites on an fcc crystal cut along the (111) axis. There are four different types of adsorption sites on this surface: a top site, a bridge site and two distinct hollow sites. The two hollow sites are distinguished by whether the adsorbate sits on top of an atom from the second atomic layer (hcp-hollow) or on top of an atom from the third layer (fcc-hollow). An adsorbate sitting on a top site is coordinated to a single surface atom, while an adsorbate in a bridge site is coordinated to
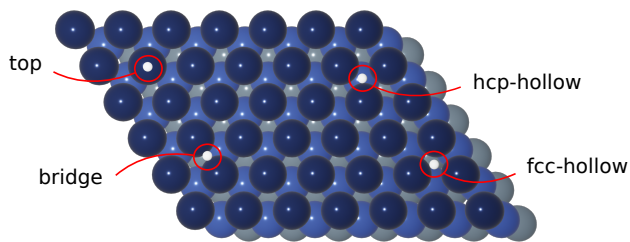
Figure 2.3: Different adsorption site on a (111) surface of an fcc crystal. The first three atomic layers of the crystal are displayed in different shades of blue and the adsorbate in white highlighted with a red circle around it.

two atoms and adsorbates in a hollow position coordinate to three or four surface atoms [7]. More complex surfaces, such a oxides, can provide multiple nonequivalent on top, bridge or hollow adsorption sites as we will see in the following section.

Let us now consider the case where two different types of adsorbates are competing for the same adsorption site. Which of these adsorbates will adsorb on the surface depends on the adsorption energy of the adsorbates on the respective adsorption site. If one of these adsorbates has a considerably higher adsorption energy, it will preferentially adsorb and if sufficiently abundant, this adsorbate will block all adsorption sites for the other type of adsorbate. This process is called surface poisoning.

In addition to surface poisoning through blockage of adsorption sites, a surface may also be poisoned by adsorbate induced structural changes. For example both Ni and Pd have been reported to undergo changes in surface structure in the presence of sulfur [8]. Ni(111) develops a (100) orientation under exposure to H_2S [9] and different Pd surfaces grow (100) facets in the presence of sulfur [8]. The phenomenon of poisoning is also discussed in the context of deactivation of industrial catalysts, which often involves the formation of a layer of inactive carbon (coke) on the active sites of the catalyst that blocks the adsorption of the reactant gases, leading to the deactivation of the catalyst by poisoning [7].

2.4   Oxide structures and surfaces

The key factors influencing an oxide's crystal structure include (i) the symmetry of the crystal lattice (as discussed earlier for metals), (ii) the stoichiometry of the oxide, meaning the relative number of the different atoms and (iii) the coordination of the different atoms (the number of oxygen atoms surrounding the metal atom and their geometrical arrangement).

Figure 2.4 illustrates the four types of metal coordination to oxygen that are mentioned
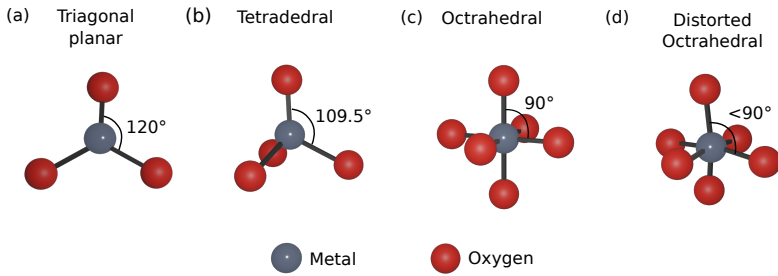
Figure 2.4: Illustrations of different coordinations of a metal atom in an oxide showing in (a) a triagonal planar configuration with 3 oxygen atoms coordinated to the metal, (b) a tetrahedral configuration with 4 oxygen atoms, an octahedral configuration in (c), and a distorted octrahedral configuration in (d).

in this thesis. Figure 2.4 (a) shows a metal in planar triagonal coordination. The metal atom is surrounded by three oxygen atoms, which are all at equal distance from the metal with a 120° angle between each pair of oxygen atoms. Figure 2.4 (b) shows a metal atom in tetrahedral coordination. The metal atom is surrounded by four oxygen atoms with a 109.5° angle between each pair of oxygen atoms. Figure 2.4 (c) illustrates an octahedral configuration in which the metal is surrounded by six oxygen atoms with equal bond length and a 90° angle between them. Figure 2.4 (d) shows a configuration called a distorted octrahedra. The central metal is coordinated to six oxygen atoms as in the octahedral configuration with a small distortion of the octrahedral shape by small deviations of some of the bond angles or lengths.

2.4.1 Indium oxide

Indium oxide is an optically transparent n-type semiconductor with a direct band gap of approximately 3 eV. In_2O_3 possesses good electrical conductivity and it has been shown that its electrical conductivity can be significantly enhanced by doping it with tin (Sn) or titanium (Ti) [10]. The doping with tin results in the transparent conductive oxide ITO (indium tin oxide), which is commonly used as a conductive thin film in various types of displays, energy efficient windows and solar cells. Other applications for In_2O_3-based materials are corrosion inhibitors in batteries, or various components in photodetectors or gas sensors [10].

In_2O_3 has two crystalline phases: cubic and rhombohedral. This thesis focuses on the cubic In_2O_3 phase. Figure 2.5 shows the unit cell of this cubic In_2O_3. The unit cell has a lattice constant of 10.12 Å and contains 32 indium atoms and 48 oxygen atoms. The indium atoms are in a 3+ oxidation state, bonded to six O^{2-} atoms in an octahedral configuration. Each O^{2-} atom is bonded to four In^{3+} atoms in a tetrahedral coordination [11, 12].
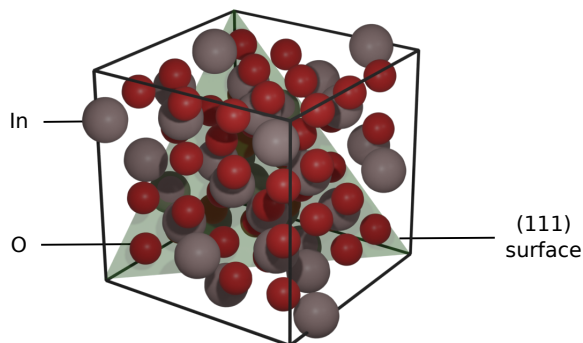
Figure 2.5: The unit cell of cubic In_2O_3. The boarders of the unit cell are shown in black, the indium atoms in gray and the oxygen atoms in red. The green plane shows how to cut the In_2O_3 crystal to obtain the (111) surface.

This thesis focuses on the (111) surface of cubic In_2O_3. The (111) surface is made by cutting the crystal along the green plane as illustrated in Figure 2.5. This imaginary cleavage of the crystal along this plane would create the ideal bulk terminated surface structure. However, this ideal bulk terminated structure does not exist in reality [13]. Cleaving the crystal leaves the top most atoms on the surface undercoordinated compared to the bulk structure, which changes their electronic structure resulting in small distortions of the surface geometry compared to the bulk structure. The resulting structure is called the relaxed surface structure.

Figure 2.6 shows the top layer of the unit cell of the relaxed $In_2O_3(111)$ surface structure. The hexagonal unit cell with a length of 14.31 Å contains 12 five-fold coordinated In atoms, 12 three-fold coordinated O atoms, 4 six-fold coordinated In(6c) atoms, and 12 four-fold coordinated O(4c) atoms [14]. The surface has 3 high-symmetry points that are labelled A, B and C.

The (111) surface has the highest thermodynamical stability among the low-index surfaces [15]. Consequently, the (111) surface is the most common surface termination of polycrystalline In_2O_3, which makes this surface termination highly interesting for surface science studies. However, growing In_2O_3 single crystals is demanding and the resulting crystals are limited to a size of approximately 1 or 2 mm making them challenging samples for area-averaging techniques [16, 17].

To overcome this size limitation of In_2O_3 single crystals, scientists started to epitaxially grow In_2O_3 films using pulsed laser deposition (PLD) and molecular beam epitaxy (MBE) [12, 18–20]. Yttria-stabilized zirconia (YSZ) is a suitable substrate for this film growth because of the relatively small mismatch of the lattice constant of In_2O_3 of 10.12 Å and double the lattice constant of YSZ (5.15 Å = 10.30Å) [21]. The $In_2O_3(111)$ films studied
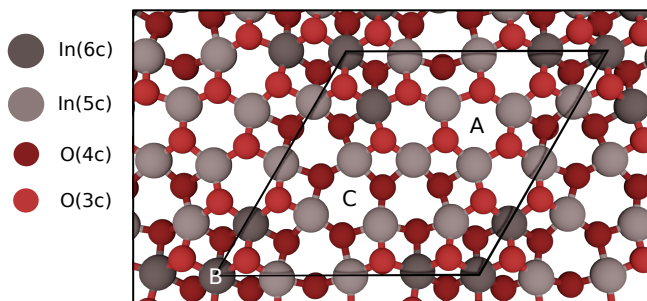
Figure 2.6: Relaxed surface structure of the In_2O_3(111) surface. The three symmetry points of the unit cell are labeled as A, B and C.

in this thesis were epitaxially grown on YSZ using a PLD process described in reference [21]. The growth method results in an atomically flat 200 nm In_2O_3(111) thin film.

2.4.2 NiMo-based oxides

The second part of this thesis focuses on the characterization of Ni- and Mo-oxide catalysts. The studied catalysts are industrial NiMo-oxide catalysts on Al_2O_3 support and NiMo-oxide nanoparticles deposited on silicon wafers. This section provides a brief overview on the crystalline structure of common Ni- and Mo-oxides. All crystalline structures that are shown in this section where drawn using atomic coordinates downloaded from 'The Materials Project' homepage [22, 23].

Ni and Ni oxides

Nickel is a ferromagnetic transition metal with the atomic number 28. Metallic Ni has a face-centered cubic (fcc) crystalline structure with the lattice constant 3.499 Å [24].

Two Ni oxides have been reported in the literature: NiO and Ni_2O_3. NiO is the stable Ni oxide that has a rock-salt structure with octahedral Ni^{2+} and O^{2-} sites [25]. Ni_2O_3, on the other hand, is much less stable and tends to decompose to NiO or form Nickel(III) oxide hydrate. Consequentially, the experimental investigation of Ni_2O_3 has been challenging, but was made possible in 2015 by the characterization of Ni_2O_3 nanoparticles [26]. Ni_2O_3 crystallizes in a monoclinic crystal system built up out of corner-sharing NiO_4 tetrahedra with two inequivalent Ni^{3+} sites.

The respective crystal structures of metallic Ni, NiO and Ni_2O_3 are illustrated in Figure 2.7.

Mo and Mo oxides

Molybdenum is a transition metal of the chromium group. Metallic Mo crystallizes in a body-centered cubic (bcc) structure with a lattice constant of 3.142 Å [24]. The bcc crystal structure is illustrated in Figure 2.8 (a).

Molybdenum forms two stoichiometric oxides which are MoO_2 and MoO_3 in which the Mo cation is, respectively, either in the 4+ or in the 6+ oxidation state. Additionally, Mo can form a range of non-stoichiometric oxides with an Mo-oxidation state between 4+ and 6+ (e.g. $Mo_{18}O_{52}$, $Mo_{11}O_{47}$, Mo_9O_{26}, Mo_8O_{23}, Mo_5O_{14}, and Mo_4O_{11}) [27].

MoO_2 has a distorted rutile (monoclinic) crystal structure [28]. The Mo^{4+} atoms bind to six equivalent O^{2-} in an octraheral coordination, while the O^{2-} atoms bind in a trigonal planar geometry to three equivalent Mo^{4+} atoms as displayed in Figure 2.8 (b).

MoO_3 forms three crystalline structures referred to as α-, β- and h-MoO_3. The β- and h-MoO_3 structures are meta-stable with a monoclinic and hexagonal symmetry [27]. Both of these MoO_3 structures decompose to α-MoO_3 at elevated temperatures [29, 30]. The only thermodynamically stable MoO_3 structure is α-MoO_3, an orthorhombic structure consisting of double layers of distorted MoO_6 octahedrals held together by covalent forces. The crystal structure of α-MoO_3 is displayed in Figure 2.8 (c).

NiMoO$_4$

Nickel and molybdenum can form a mixed oxide nickel molybdate with Ni^{2+} and Mo^{6+}. This oxide exists in two crystalline forms α-$NiMoO_4$ and β-$NiMoO_4$, which are displayed in Figure 2.9 (a) and (b), respectively. The two structures are distinguished primarily by the coordination of the Mo^{6+}, which is octahedral in the α-phase and tetrahedral in the β-phase [31, 32]. α-$NiMoO_4$ is the low temperature oxide. The β-phase is formed by heating α-$NiMoO_4$ to a temperature of 700 °C and the β-$NiMoO_4$ is, subsequently, meta stable to a temperature of 180 °C [33, 34].

The industrial $NiMoO_x$ catalysts studied in this thesis were synthesized by incipient wetness impregnation of δ-Al_2O_3. The structure of the resulting $NiMoO_x$/Al_2O_3 catalysts are not as clearly defined as the structure of the $In_2O_3(111)$ model catalysts and the specific surface termination of the $NiMoO_x$ catalyst was not further investigated.
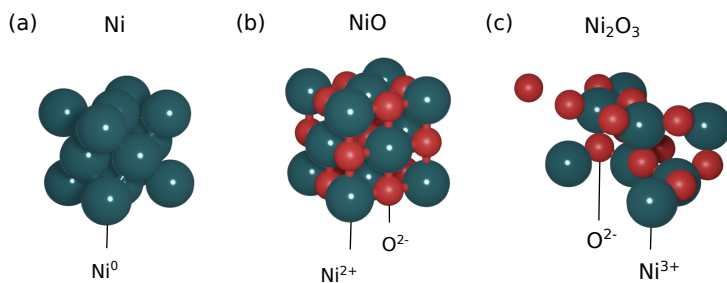
Figure 2.7: Crystal structures of (a) metallic Ni, (b) NiO and (c) Ni_2O_3 with the corresponding oxidation states of the different atoms.
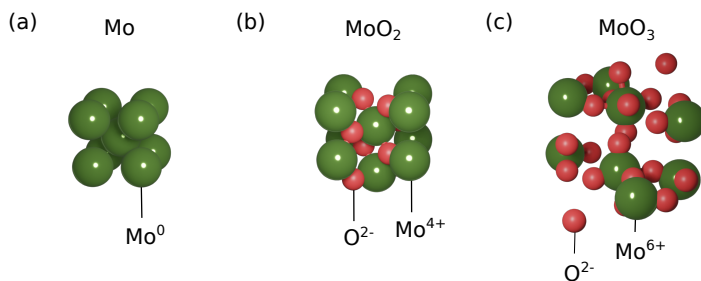
Figure 2.8: Crystal structures of (a) metallic Mo, (b) MoO_2 and (c) MoO_3 with the corresponding oxidation states of the different atoms.
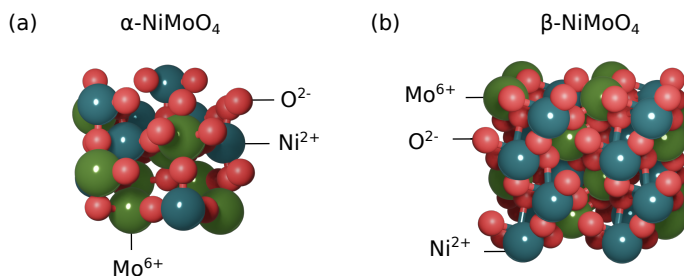
Figure 2.9: Crystal structures of the two crystalline phases of $NiMoO_4$: (a) α-$NiMoO_4$ and (b) β-$NiMoO_4$ with the corresponding oxidation states of the different atoms.

Chapter 3

Catalysis

In the previous chapter we discussed the geometrical arrangement of atoms in the bulk and on the surfaces for the oxides studied in this thesis and how molecules can adsorb on surfaces. All of this was discussed from a fundamental point of view. The following chapter will focus on a more applied side of catalysis research. The first section discusses how catalysts facilitate chemical reactions. The second section focuses on the relationship between surface science and applied catalysis research and the two fundamental gaps between these two research fields, the materials and the pressure gap. Finally, we will have a look at applications of the two catalytic materials studied in this thesis In_2O_3 and NiMo-oxides.

3.1 Surface reactions in heterogeneous catalysis

As discussed in the introduction, a catalyst is a substance that takes part in a chemical reaction without being consumed during the reaction. Instead, the catalyst takes the role of an active chemical spectator that facilitates the reaction. [1] In this section, we will examine the interaction between catalysts and the reactants.

Let us consider a basic reaction involving two reactants, denoted as X and Y. These reactants X and Y react to form a reaction product Z:

$$X + Y \rightarrow Z \tag{3.1}$$
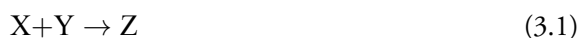
To make this reaction possible, one or both of the reactants might have to dissociate and new chemical bonds are formed. This breaking and forming of new chemical bonds requires a certain amount of energy, known as the activation energy E_{act} of the reaction. A
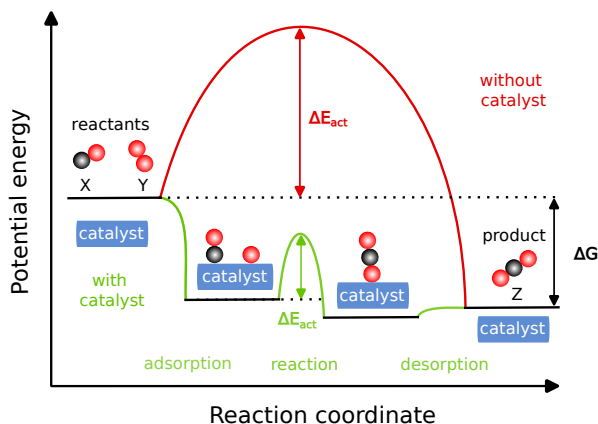
Figure 3.1: Illustration of the potential energy of a simple chemical reaction under the influence of a catalyst. The required activation energy for the reaction process is lowered by the addition of a catalyst, while the energy difference between reactants and products (Gibbs free energy △G) remains the same. Figure adapted from reference [1, 35].

catalyst facilitates the chemical reaction by lowering the activation energy for the reaction, by providing an alternative reaction pathway on its surface that is energetically favourable over a reaction without a catalyst.

Figure 3.1 illustrates the potential energy of a chemical reaction with and without a catalyst. A chemical reaction involving a catalyst can be divided into three steps. First, one or multiple of the reactants adsorb on the catalyst's surface, which can involve the dissociation of the adsorbed reactants on the surface. In the second reaction step, the reactants need to overcome the activation energy barrier E_{act} to form the reaction product. The interaction of the reactants with the catalyst has lowered this activation barrier considerably compared to the reaction without a catalyst. In the final reaction step, the reaction product desorbs from the surface.

The potential energy difference between the reactants and the product desorbed from the catalyst is identical to the potential energy difference between the reactants and the product obtained without a catalyst. Thus, the catalyst lowers only the activation energy, but the potential energy difference between reactants and products remain unchanged. For more complicated chemical reactions with multiple possible reaction products, catalysts are also used to guide the reaction along the desired reaction pathway, and thus increase the selectivity towards the desired product.

Three types of catalytic reaction mechanisms are typically discussed, (i) the Langmuir-Hinshelwood, (ii) the Eley-Rideal and (iii) the Mars-van Krevelen reaction mechanism. The three mechanisms are illustrated in Figure 3.2. In a Langmuir-Hinshelwood reaction,
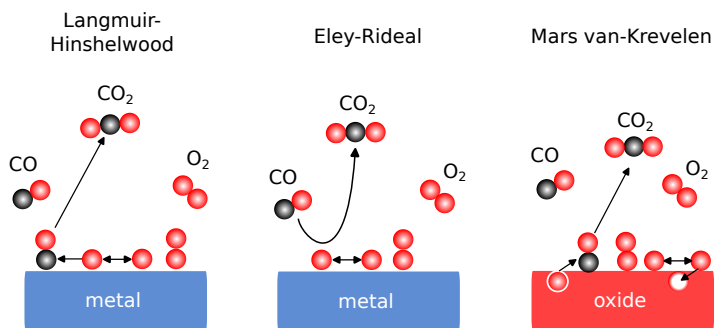
Figure 3.2: Schematic illustration of the three reaction mechanisms in heterogeneous catalysis: the Langmuir-Hinshelwood, the Eley-Rideal and the Mars van-Krevelen reaction mechanism. Illustrated on the example of CO oxidation to CO_2.

both reactants adsorb to the surface and their reaction on the surface is the rate determining step of the reaction. In the Eley-Rideal mechanism, only one of the reactants is adsorbed on the surface, while the other reactant remains in the gas phase. The Mars-van Krevelen reaction mechanism involves the reduction and formation of an oxide, which is reduced by the reaction and subsequently rebuild.

Catalysis research tries to identify the so-called active sites of a catalyst. These are the adsorption sites at which the catalytic reactions take place. For the surfaces of many transition metals, coordinatively unsaturated (cus) metal and oxygen sites have been proposed as active sites [13, 36]. These cus sites are created when an oxide surface cleaves the metal-oxygen bond. After the cleavage, metal and oxygen atoms have a coordination vacancy and can serve as electron donors or acceptors. In oxidation reactions, undercoordinated oxygen atoms are less strongly bond to the lattice and can be removed from the lattice more easily. The role of cus sites in the activity of oxide catalysts has been investigated for multiple transition metal oxides such as RuO_2 and IrO_2 [37].

While surface science often talks about the coordination of atoms to each other, applied catalysis research describes catalysts in terms of charge transfer between the catalyst and the adsorbates rather than in terms of atomic coordination. A terminology that is often used in this context are acidity and basicity analogous to the usage of these terms in wet chemistry. A Lewis acid site of a catalyst receives an electron from the adsorbate. On a Brønsted site, on the other hand, the charge transfer takes place via the exchange of a proton and a Brønsted acid site donates a proton to the adsorbate [38].
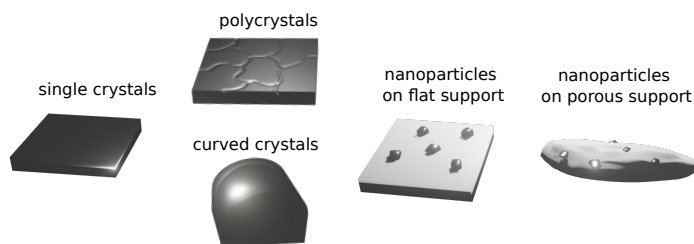
Figure 3.3: Illustration of the materials gap between surface science and catalysis. Showing a single crystal on the left, more complex model systems such a polycrystaline surfaces, a curved crystal and ordered nanoparticles in the middle and nanoparticles on a porous support on the right.

3.2 The materials and pressure gap

Industrial processes use catalysts consisting of supported nanoparticles and operate at high pressures. In surface science, on the other hand, experiments are traditionally conducted on idealized single crystalline surfaces and at very low pressures. These apparent differences in operational conditions result in two fundamental gaps between surface science investigations and industrial catalysis, and are referred to as the materials and the pressure gap. Surface scientists try to bridge these two gaps by studying samples of higher complexity than single crystals (see Figure 3.3) and by the continuous development of experimental techniques to extend the pressure range at which experiments can be conducted.

3.2.1 The materials gap

In traditional surface science experiments, single crystalline surfaces of catalytic materials are used to model individual facets of the supported nanoparticles in industrial catalysts. Experiments on the simplified model catalysts provide detailed information about the adsorption sites, surface structure and reaction mechanism on the respective model surface. However, the measurements are limited to one surface at a time. It is possible to selectively choose the surfaces that occur most frequently in industrial catalysts or select the surfaces predicted to be catalytically most active based on calculations. However, experiments limited to one surface orientation at a time undeniably have disadvantages, since measuring multiple surfaces is time consuming and comparison between different surfaces can be challenging, since the surfaces might not be comparable due to differences in temperature measurements or cleanliness of the experimental chamber.

To overcome this limitation of measuring one crystal facets at a time, samples with multiple facets have become more popular in surface science experiments in recent years, since these samples allow for a direct comparison of the different crystal facets. The two most

commonly studied samples are polycrystaline foils [**F**, **J**, 39, 40] and curved crystals [**I**, 41]. Curved crystals are single crystals that have been polished to create a curved surface. This curved surface exhibits different surface orientations along the curvature. Mapping the surface orientation with techniques such as Low Energy Electron Diffraction (LEED) or Electron BackScatter Diffraction (EBSD) allows to correlate the experimentally observed surface properties to the surface orientation. Thus, curved crystals or polycrystaline foils allow to compare the behaviour of different surface orientations. However, they do not provide insights into the interaction of the catalytic material with its support.

Industrial catalysts typically consist of small nanoparticles deposited onto a porous support. The most common deposition technique is incipient wetness impregnation, which was also used for the catalysts studied in this thesis. In this deposition method, the support is impregnated using a precursor-containing solution. Subsequently, the catalyst is dried and later activated through calcination and/or reduction treatment. For industrial usage the catalyst is often processed further by applying the catalyst to a monolith or pressing it into tablets or pellets.

The interaction between the catalytic material and its support can be studied using deposited nanoparticles on flat substrates such as wafers or foils of the respective support material. The nanoparticles often have a wide range of different crystal facets, which, on one hand, makes them much more similar to industrial catalysts but, on the other hand, makes it much more challenging to correlate observed effects to the different facets. Nanoparticles can be grown using a range of different techniques allowing of various degrees of control of the nanoparticle size, density and composition.

In this thesis, we studied the effect of the materials gap on NiMo-oxide catalysts and investigated the potential of different model systems for the NiMo-oxide catalysts. Manuscript [**III**] explores Ni and Mo foils as model systems for $NiMoO_x/Al_2O_3$ catalysts and manuscript [**IV**] studies $NiMoO_4$ nanoparticles as an alternative model system.

3.2.2 The pressure gap

Historically surface science experiments have limited themselves primarily to Ultra High Vacuum (UHV) conditions. On one hand, this is motivated by the fact that these low pressures allow good control of the experimental conditions, which is often a prerequisite for fundamental surface science studies on gas adsorption, surface coverage and surface reconstruction. On the other hand, many classical surface science techniques are based on the detection of electrons and are therefore limited by the mean free path of electrons. The mean free path of electrons is quite short at elevated pressures, which limits the pressure range of these techniques. Due to this, surface science experiments using these techniques were initially limited to *ex situ* studies. Meaning that model catalysts could be studied

before and after exposure to gases but not during the exposure to the gases.

However, technological advancement in recent years have enabled us to carry out experiments with some of these UHV techniques at elevated pressures, allowing us to study catalysts in interaction with gases *in situ*. Examples for these technological advancements are the development of Ambient Pressure X-ray Photoelectron Spectroscopy (APXPS) [42] and High-Pressure Scanning Tunneling Microscopy (HPSTM) [43].

3.3 Indium oxide catalysts for CO_2 hydrogenation

The hydrogenation of CO_2 to methanol is a promising pathway towards the reduction of CO_2 in the atmosphere and the renewable production of methanol. Methanol can be used as an alternative fuel or fuel additive for combustion engines where battery based solutions are impractical due to their low volumetric and gravimetric energy density [44]. Methanol is also a key building molecule in the chemical industry, since it is the feedstock for formaldehyde, which is used in the production of resins, plastics, disinfectants, cosmetics and pharmaceuticals. With a yearly production of approximately 30 megatons, formaldehyde is one of the most important chemical products worldwide [45].

The high demand for methanol makes the methanol synthesis by CO_2 hydrogenation attractive from an economical point of view. Additionally, the potential to synthesize methanol from CO_2 obtained from carbon capture and green hydrogen obtained from renewable water splitting makes catalytic methanol synthesis equally appealing from an environmental point of view. Over the years, a range of different catalysts have been studied for hydrogenation of CO_2 to methanol [46]. While CuZn-based catalysts remain the industrial standard [47, 48], alternative catalysts have received a lot of attention in recent years, and In_2O_3 is one of them.

In_2O_3 on ZrO_2 support has sparked great interest due to its high selectivity for methanol synthesis [49]. The high selectivity was attributed to the creation and annihilation of oxygen vacancies that were suggested as active sites. However, the high selectivity was only observed at relatively low temperatures. At temperatures exceeding 330 °C, the conversion rate of CO_2 continues to increase. The methanol yield, however, diminishes due to the production of CO through the competing reverse water gas shift (RWGS) reaction [50]. The precise mechanism responsible for this temperature-dependent selectivity of the catalysts is still a subject of scientific debate [51].

In a recent *in situ* study, Zhang et al. investigated surface reconstructions of In_2O_3/ZrO_2 catalysts during CO_2 hydrogenation reactions [52]. The authors report that partially reduced In_2O_3 migrates in and out of the subsurface of the ZrO_2 support under reaction conditions. At elevated temperatures less partially reduced In_2O_3 was observed on the sur-

face, was accompanied by a significantly lower selectivity toward methanol and increased selectivity towards CO. Additionally, the authors point out that there is an optimum surface coverage of partially reduced In_2O_3 and O-vacancies on the surface under reaction conditions. Based on their observations, the authors conclude that the activity and selectivity of the In_2O_3/ZrO_2 is not solely determined by O-vacancies in the In_2O_3 but also strongly correlated to the interaction of the In_2O_3 with the ZrO_2 support.

Furthermore, it has been shown that the activity of In_2O_3-based catalysts can be increased by promoting the In_2O_3/ZrO_2 catalysts with Pd [53]. The role of the Pd promotor is to facilitate the process of hydrogen splitting in the hydrogenation reaction. However, the promotion with Pd requires a highly controlled growth process to grow the desired Pd-nanostructure, since otherwise the incorrectly grown Pd nanoparticles facilitate the parasitic RWGS reaction, reducing the catalysts selectivity towards methanol. An additional study showed that the selectivity and stability of Pd-promoted In_2O_3/ZrO_2 catalysts can be improved further by wet impregnation of the Pd promotor [54].

Additional fundamental studies on well-defined, crystalline In_2O_3 surfaces could advance our understanding of the CO_2 hydrogenation reaction over In_2O_3-based catalysts. Some computational studies on CO_2 hydrogenation over well-defined crystalline In_2O_3 surfaces can be found in the literature [15, 55–59]. However, very few experimental studies on single crystalline In_2O_3 surfaces have been published. The lack of experimental investigations is mainly due to the difficulty in producing well-ordered single-crystalline In_2O_3 surfaces for the experiments. This thesis contributes to the discussion on In_2O_3 surfaces with two surface science studies on the $In_2O_3(111)$ surface, which can be found in manuscript [I] and [II].

The (111) surface termination was chosen for our experiments, because it is the thermodynamically most stable low index In_2O_3 surface and has been identified as an active surface for CO_2 hydrogenation [15]. A few years ago, Frei et al. published a combined Microkinetics and DFT study on CO_2 hydrogenation over the $In_2O_3(111)$ surface [15]. They proposed a reaction mechanism with one O-vacancy per unit cell where one CO_2 molecule adsorbs next to the O-vacancy and is, subsequently, protonated by co-adsorbed hydrogen. The proposed reaction intermediates are formate (HCOO), formic acid (HCOOH), H_2COOH, methanediol (H_2COHOH), physisorbed formaldehyde (H_2CO), methoxy (H_3CO) and H_3COH. However, these O-vacancies have not been observed on $In_2O_3(111)$ in surface science experiments. Instead the reduction of the $In_2O_3(111)$ surface results in the formation of an ordered array of indium adatoms with one adatom per unit cell [14]. This has caused some debate about the suggested O-vacancy driven reaction mechanism.

This thesis presents two surface science studies on the interaction of CO_2 with $In_2O_3(111)$. Manuscript [I] is a study on CO_2 adsorption on different terminations of the $In_2O_3(111)$ surface. The combined experimental and theoretical study shows how dissociated water

on the surface blocks the adsorption of CO_2. The next manuscript [II] investigates the interaction of CO_2 with the $In_2O_3(111)$ surface at elevated pressures and studies the poising effect of sulfur-based contamination on the surface.

3.4 NiMo-oxide catalysts for hydrodeoxygenation reactions

Mo-based catalysts have been used in hydrotreating processes for the upgrading of highly contaminated crude oil to quality fuels and other products for many years [60]. These hydrotreating processes are necessary to reduce the amount of sulfur, nitrogen, oxygen and metallic contaminants in the crude oil and can also be employed to convert aromatics and olefins in crude oil to saturated hydrocarbons [61]. In more recent years, the decreasing global fossil fuel resources combined with growing concerns about the rising levels of greenhouse gases in the atmosphere have driven research and industry to work towards more sustainable fuel sources.

The upgrading of biomass has been identified as a promising way to decrease the dependence on fossil fuels by establishing a more sustainable fuel production. However, today's biofuels, such as biodiesel or bioalcohols, are synthesized from edible commodities such as sugars, starch, or vegetable oils, and thus pose a competition to actual food for valuable farm land [62]. An alternative solution for the synthesis of renewable fuels is the production of biofuels from plant-based waste products such as lignin, which is a by-product of the pulp and paper industry [63, 64]. Lignin is an abundant, large oxygenated aromatic polymer that can be upgraded by catalytic hydrodeoxygenation (HDO) [65]. HDO is the removal of oxygen from a oxygen-containing compound by hydrogen. Since the HDO process of lignin is similar to the deoxygenation of crude oil, the hydrotreatment of lignin with MoO_x/Al_2O_3-based catalysts has been explored as a way to upgrade lignin and has shown promising results [66].

The activity of Mo-based catalysts in HDO reactions has been attributed to undercoordinated Mo^{5+} sites on which the oxygenate is activated [67]. It has been shown that the activity of the MoO_x/Al_2O_3 catalysts can be improved by adding metal promoters such as Ni, Co or W [68, 69]. These promoters donate additional electrons to the Mo facilitating the formation of undercoordinated Mo sites [69].

The industrial $NiMoO_x/Al_2O_3$ catalysts are typically synthesised using incipient wetness impregnation and are subsequently sulfidised. This sulfidation results in the formation of MoS_2 nanoclusters whose edges are active sites for HDO reactions [70–73]. The active sites of MoS_2 are sulfur vacancies that result in undercoordinated Mo sites.

This thesis focuses on unsulfidized $NiMoO_x/Al_2O_3$ catalysts, which are subsequently referred to as $NiMo/Al_2O_3$ catalysts. In particular, the H_2 reduction of $NiMo/Al_2O_3$-based

catalysts and model systems of these catalysts were studied under *in situ* conditions. These fundamental studies on the behavior of these materials provide insights into the properties of the catalysts and the suitability of the tested model systems. In the future, these fundamental investigations on the reduction of these catalysts will hopefully provide a foundation for more applied studies.

The reduction of $NiMo/Al_2O_3$ catalysts has been studied by H_2 Temperature Programmed Reduction (TPR) for a long time [74, 75]. These studies reported a correlation between the reducibility of Mo-based catalysts and their activity. An increased activity could be correlated to a lower reduction temperature. The reduction temperature of Mo/Al_2O_3 catalysts has been reported to decrease with increasing Mo loading as long as the Mo is amorphous [76]. Pure Ni/Al_2O_3 catalysts typically have a slightly higher reduction temperature than pure Mo/Al_2O_3 catalysts [76]. The Ni/Al_2O_3 TPR spectrum often shows two distinct peaks that are assigned to the reduction of surface and bulk Ni [77]. While TPR provides insights into how metal loading or calcination of monometalic catalysts influences their reduction behavior, the interpretation of TPR data of bimetalic catalysts is more challenging. TPR studies on bimetallic $NiMo/Al_2O_3$ catalysts showed that Ni and Mo facilitate each other's reduction [77]. It is, however, challenging to obtain detailed insights into the reduction mechanism from pure TPR studies, since the technique studies the reduction of the whole catalysts and lacks sensitivity for the different elements. In order to close this knowledge gap, we performed *in situ* measurements of the reduction of $NiMo/Al_2O_3$ catalysts with element specific techniques such Ambient Pressure X-ray Photoelectron Spectroscopy (APXPS) and X-ray Adsorption Spectroscopy (XAS) and combined these with *ex situ* Transmission Electron Microscopy (TEM) and X-Ray Diffraction (XRD) measurements.

In manuscript [III] we investigate how the composition of $NiMo/Al_2O_3$ and the interaction of the catalytic materials with the Al_2O_3 support affects the reduction of the catalysts in H_2. We tested the suitability of Ni- and Mo-foils, and monometallic Ni/Al_2O_3-catalysts and Mo/Al_2O_3-catalysts as model systems for the $NiMo/Al_2O_3$-catalysts. The experiments show that the tested model systems behave differently to the $NiMo/Al_2O_3$-catalyst, which severely limits their suitability as a model system. This highlights the need to develop better model systems for $NiMo/Al_2O_3$-catalysts.

NiMo nanoparticles produced by spark discharge have been suggested as a model system for $NiMo/Al_2O_3$ catalysts in the literature [78]. We studied such a model system in manuscript [IV] and tested its suitability as a model system by comparing the reduction of these nanoparticles to the reduction of the $NiMo/Al_2O_3$-catalysts studied in manuscript [III]. It can be concluded that the nanoparticles investigated in manuscript [IV] are a better model system for the $NiMo/Al_2O_3$-catalysts than the foils tested in manuscript [III].

Additionally, the effect of noble metals on the $NiMo/Al_2O_3$-catalysts was studied in manuscript [V]. Different noble metals have been reported to promote reduction reactions over

Mo-oxide-based catalysts by activating hydrogen that, subsequently, spills over to the Mo oxide [79, 80]. Manuscript [**v**] investigates, in particular, the promotion effect of Ru and Pd. The experiments focus on the reduction NiMo/Al$_2$O$_3$-catalysts promoted with these noble metals. The *in situ* studies in manuscript [**v**] show that the addition of the noble metals has a significant effect on the reduction of the NiMo/Al$_2$O$_3$-catalysts and different characteristics could be observed for Pd- and Ru-based promotion.

Chapter 4

Methods

The following chapter discusses the experimental and computational methods used in the thesis. The first part of this chapter focuses on X-ray based techniques. As an introduction to the X-ray based techniques, the first section start with a brief discussion on how X-rays are generated by a synchrotron light source. The following two sections discuss the two synchrotron-based techniques that were used in this thesis, X-ray Photoelectron Spectroscopy (XPS) and X-ray Absorption Spectroscopy (XAS). The subsequent sections provide a brief introduction to the non-X-ray based methods that were used in this thesis. These techniques were Diffuse Reflectance Infrared Fourier Transform Spectroscopy (DRIFTS), Transmission Electron Microscopy (TEM), Low Energy Electron Diffraction (LEED) and Temperature Programmed Reduction (TPR). Finally, the last section in this chapter gives a very brief introduction to Density Functional Theory (DFT) calculations, which were used to analyze the XPS data.

4.1 Synchrotron Light Sources

The most common X-ray light sources are synchrotron light sources and X-ray tubes. Inside an X-ray tube, an electron beam is shot onto a metal target to excite core-level electrons of the metal target. This leaves the metallic atoms in an electronically excited state. In the relaxation process, electrons from the outer electron shells fill the core-level vacancies and X-ray photons are emitted. This process is known as X-ray fluorescence. The emitted X-rays have discrete energies determined by the electronic states of the metal target. These characteristic X-rays can be used for experiments. Additional to the fluorescence X-rays, a broad band spectrum of X-rays is created by the Bremsstrahlung of the electron beam that is shot onto the metal target. The intensity of the X-rays created by Bremsstrahlung is
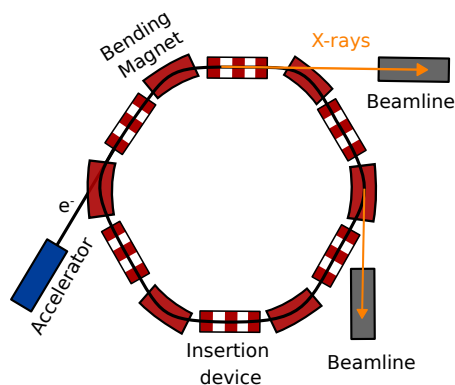
Figure 4.1: Illustration of the storage ring of a synchrotron. Figure adapted from reference [81].

typically much lower then the intensity of the X-ray fluorescence lines, consequently most X-ray tube setups use the X-ray fluorescence lines for the measurements.

On the other hand, synchrotron light sources generate X-rays purely from Bremsstrahlung. Synchrotron light sources are particle accelerators, in which the X-rays are created by the deceleration of electrons within magnetic fields. Figure 4.1 shows a schematic illustration of a synchrotron storage ring. The electrons are typically generated outside of the storage ring and accelerated to a speed close to that of the speed of light, before they are injected into the storage ring. The synchrotron storage ring itself consists of different units that keep the electrons on a closed loop trajectory. As the electrons travel through the storage ring, they are decelerated by the magnetic fields of bending magnets, undulators and wigglers. This deceleration causes the electrons to emit X-rays in the form of Bremsstrahlung. These X-rays are used for the experiments at a synchrotron.

The properties of the magnetic fields that the electrons interact with, greatly affects the spectrum of the emitted X-rays. Figure 4.2 shows a sketch of the design of a bending magnet compared to that of an undulator and their resulting X-ray emission spectra. The bending magnet consists of a single pair of magnets resulting in a wide curve deflection of the electrons. This electron path gives rise to a broad spectrum of emitted X-rays. An undulator, on the other hand, consists of a stack of magnets with alternating polarity that causes the electrons to oscillate back and forth. Whenever the electrons are decelerated within the undulator, they emit X-ray radiation. The different bunches of radiation interfere with each other, resulting in an X-ray spectrum with distinct peaks called harmonics. These insertion devices typically provide radiation of much higher intensity than bending magnets.

Synchrotron light sources have a couple of advantages over lab sources with X-ray tubes. First, the fact that the X-ray emission spectrum of an electron beam is depended on the properties of the magnetic field allows to generate X-rays of a wide range of photon energies
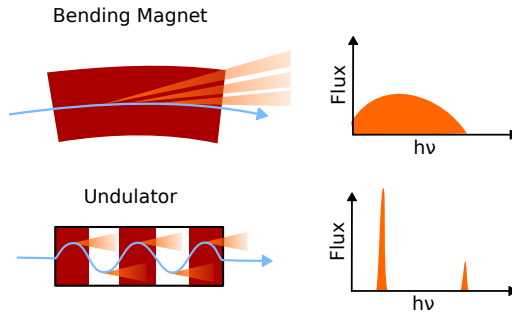
Figure 4.2: Sketch of the X-ray radiation emitted from bending magnets and undulators and their corresponding emission spectra. Figure was adapted from reference [82].

by tuning the magnetic field. Therefore, a synchrotron light source allows to adjust the energy of the radiation and can generate photons with an energy ranging from UV light to hard X-rays. Modern synchrotron sources are also much more brilliant than standard X-ray tubes, meaning that synchtron-based X-rays have a higher number of photons per unit of time, area, emission angle and bandwidth.

The synchroton-based measurements presented in this thesis were done at the MAX IV synchrotron light source at the FlexPES, HIPPIE and Balder beamline, and at the Diamond Light Source at the b07 beamline. The Diamond Light Source is a third generation synchrotron that has been in operation since 2007. MAX IV is the world's first fourth generation synchrotron and operates two storage rings that run with an energy of 1.5 GeV and 3 GeV, respectively.

4.1.1 Anatomy of a beamline

Once the X-rays have been generated by the insertion device, they enter the so-called beamline. The typical elements of a beamline are shown schematically in Figure 4.3, which depicts the layout of the HIPPIE beamline at MAX IV. On the left, we see the Elliptically Polarizing Undulator (EPU) unit in which the X-rays are generated by passing the electrons through a magnetic field as discussed above. The X-ray beam from the undulator passes through the beamline onto the first mirror that is called M1 in Figure 4.3. This first mirror adsorbs a considerable amount of the heat load of the X-ray beam and collimates the beam unto the monochromator. The monochromator is needed to select the desired energy of the X-rays by filtering out all other energies. Figure 4.3 displays a Plane Grating Monochromator (PMG). Inside the PMG is a grating that diffracts the polychromatic X-ray beam. The diffraction angle of the X-rays is energy depended following Bragg's law. The polychromatic X-ray beam is thus spectrally dispersed and the desired X-ray energy
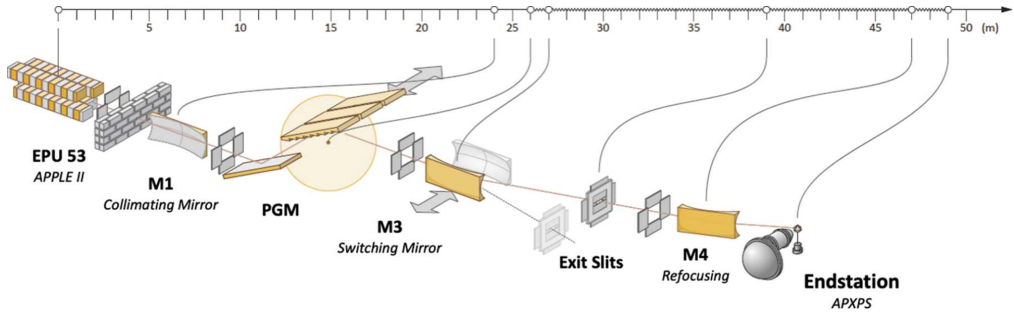
Figure 4.3: Illustration of the main elements in a synchrotron beamline, shown by the example of the HIPPIE beamline at MAX IV. Adapted from reference [51].

can be selected by passing the beam through a slit behind the diffraction grating. Behind the monochromator is the exit slit that can be used to optimize the energy resolution of the X-ray beam and a final mirror that focuses the beam onto the sample.

4.2 X-ray Photoelectron Spectroscopy

The following section is an introduction to X-ray Photoelectron Spectroscopy (XPS), which is the main experimental technique used in this thesis. The first subsection discusses the underlying physical principles on which the technique is based. The second section introduces the technical basics of an XPS instrument and how to modify such a setup in order to measure at elevated pressure.

4.2.1 Basic Principle

X-ray Photoelectron spectroscopy (XPS) is an experimental technique that gives information on the atomic composition of materials. The technique is based on the photoemission process, illustrated in Figure 4.4 (a): An atom is excited by the absorption of an incoming X-ray photon that excites a core-level electron into the continuum, leaving behind a core hole in the atom. The excited electron is then referred to as a photoelectron since it was created by the photoelectric effect. Photoelectron spectroscopy measures the kinetic energy of these photoelectrons E_{kin}. Based on the kinetic energy, one can calculate the initial binding energy of the photoelectrons E_{bin} with the equation below:

$$E_{\text{bin}} = h\nu - E_{\text{kin}} - \phi \qquad (4.1)$$

where $h\nu$ is the energy of the incoming photon with frequency ν, h is Planck's constant
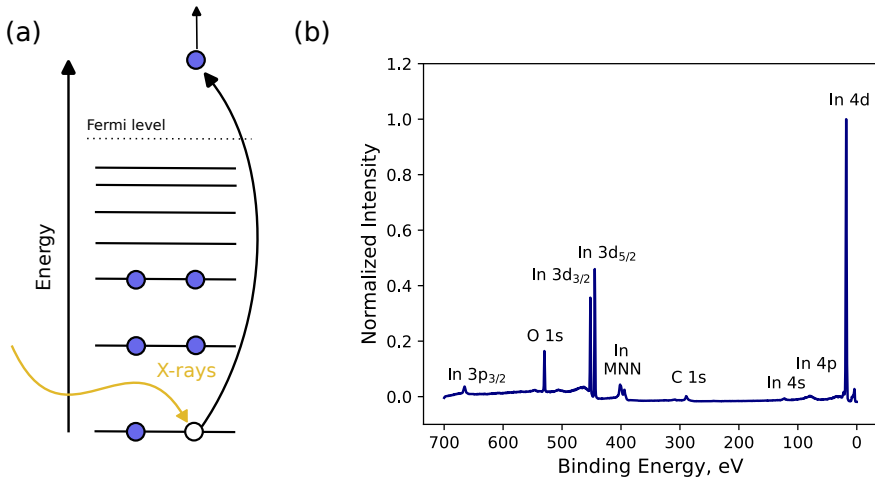
Figure 4.4: Panel (a) shows a simple illustration of the photoemission process where a core level electron is excited into the continuum after the absorption of an X-ray photon. Panel (b) displays an XPS spectrum from an In_2O_3(111) surface measured with a photon energy of 800 eV. The spectrum shows photoelectron and Auger peaks from a scan over a wide range of energies.

and ϕ is the workfunction of the surface that the photoelectron needs to overcome to be emitted into vacuum. The binding energies obtained from the kinetic energies of the photoelectrons are element specific and thus give information on the elemental composition of the investigated sample.

Figure 4.4 (b) depicts an XPS survey spectrum of In_2O_3. The spectrum shows photoemission and Auger peaks that can be assigned to indium, oxygen and carbon core levels. The background signal is created by scattered electrons. When analysing XPS data in detail the background is subtracted from the spectrum and the shape of the photoelectron peak is fitted with a function consisting of a Gaussian and a Lorenzian contribution. The simplest background is a linear background but often a Shirley or Tougaard background is used [84, 85].

The XPS core level peaks are labelled as nl_j where n is the principal quantum number, l is the angular momentum and j is the total angular momentum. The total angular momentum j is defined as

$$|l - s| \leq j \leq |l + s| \tag{4.2}$$

with the electron spin s that can take values of either $+\frac{1}{2}$ or $-\frac{1}{2}$. The two possible values of s result in two j values for all orbitals with $l \neq 0$. These different j values can have different energies that can be observed as a doublet signal in the XPS spectrum. An example of
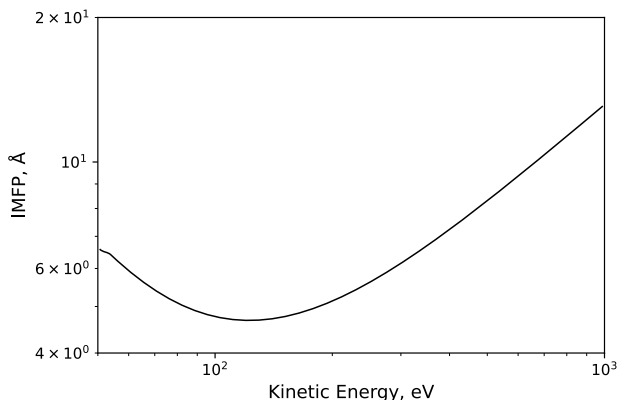
Figure 4.5: The IMFP of electrons in gold as a function of the electron's kinetic energy. The IMFP was calculated using the TPP-2M equation [83].

this can be seen for the In 3d peak in Figure 4.4 (b). This effect is known as spin-orbital splitting. The doublet peaks have specific area ratios based on the level of j degeneracy, i.e. 2:1, 3:2 and 4:3 for p, d and f orbitals, respectively.

Once the photoelectrons have been emitted from the atoms, they can only travel a limited distance through the material before they are scattered by the atoms in the material. The average distance that an electron can travel without experiencing any scattering is referred to as the inelastic mean free path (IMFP). Figure 4.5 shows a plot of the IMFP of electrons as a function of their kinetic energy. According to the figure, the IMFP of an electron with a kinetic energy of 1000 eV is approximately 15 Å and will be even lower for lower kinetic energies. This effect significantly limits the escape depth of photoelectrons from the sample and gives XPS its high surface sensitivity.

XPS can be used to measure small changes in the binding energy of electrons that are caused by changes in the chemical environment of the atom. Figure 4.6 (a) illustrates an example of how XPS can be used to obtain chemical information of a material. The figure shows two Mo 3d spectra of Mo-foil. Molybdenum can form many different chemical compounds in which the Mo-atoms can take oxidation states from 6+ to 2-. The spectrum at the bottom of Figure 4.6 (a) shows an oxidized Mo-foil and the top spectrum shows a metallic Mo-foil. The two core level spectra both show the typical $3d_{5/2}$ and the $3d_{3/2}$ doublet with the 3:2 intensity ratio. The oxidized Mo-foil has a Mo $3d_{5/2}$ peak at a binding energy of 232.5 eV. This binding energy corresponds to Mo^{6+} from MoO_3. Additionally, the oxidized foil shows a small shoulder at approximately 231.2 eV, which indicates a small amount of Mo^{5+} in the foil. The spectrum of the metallic foil shows a Mo $3d_{5/2}$ peak with a binding energy of 228.2 eV. This binding energy is in good agreement with the binding energy of metallic Mo^{0+}.
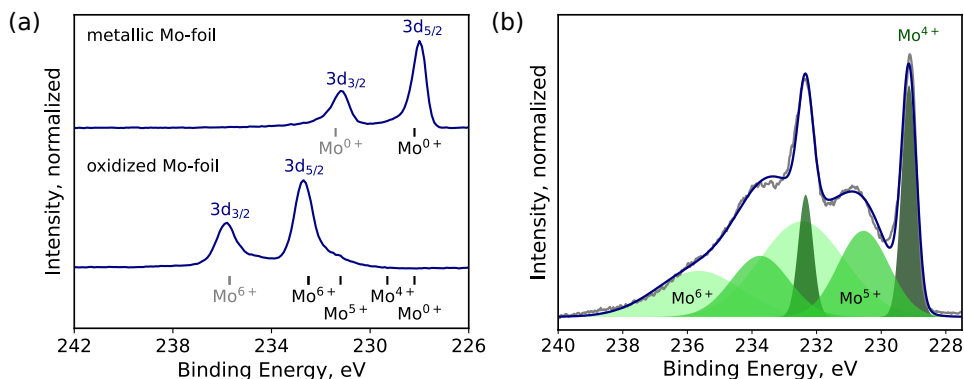
Figure 4.6: (a) Mo 3d core level spectra of oxidized and metallic Mo-foil to illustrate the concept of chemical shifts in XPS spectra. The binding energies of the different Mo-oxidation states is marked underneath the spectra. The binding energies for the $3d_{5/2}$ core level are marked in black and the binding energy of the $3d_{3/2}$ are marked in gray. (b) An XPS fit of the Mo 3d core level spectrum of a partially reduced Mo-oxide foil.

The oxidation state of the two Mo foils in Figure 4.6 (a) can be identified quite clearly by looking at the spectra and comparing the measured binding energy of the XPS peaks to literature values. However, to gain a quantitative understanding of the ratios of the different oxidation states in the foils, the spectra need to be analyzed more carefully. This is can be done by fitting the spectra. Figure 4.6 (b) shows the fit of a Mo 3d spectrum from a partially reduced Mo-oxide foil. Mo^{6+}, Mo^{5+} and Mo^{4+} can be detected in the material. The ratio of the area of the functions for the different oxidation states is proportional to the distribution of the oxidation states in the material.

To fit an XPS spectrum, the position and width of the peak have to be constrained, and a fit function has to be chosen to fit the individual peaks. The peak positions are constrained based on reference measurements or reference calculations of known materials. The peak width is depended on how well-ordered a system is, the lifetime of the core hole and experimental parameters. Well-ordered systems such as metals or gases give sharper peaks than less ordered systems such as the oxides studied in this thesis.

There are different types of fit functions for XPS peaks. Most of these functions are a mixture of a Gaussian and a Lorentzian contribution. The Gaussian contribution is associated with the experimental and thermal broadening of the XPS peak, and the Lorentzian broadening originates from the lifetime broadening of the measured final state. There are different ways to combine a Gaussian and a Lorentzian contribution in a function. The common opinion is that the convolution of a Gaussian and a Lorentzian in the form of a Voigt function is the most physically accurate way to fit XPS spectra. However, many solids particularly oxides have many electronic states with very similar energies, which can make a single Voigt function a non-ideal choice for fitting such spectra.
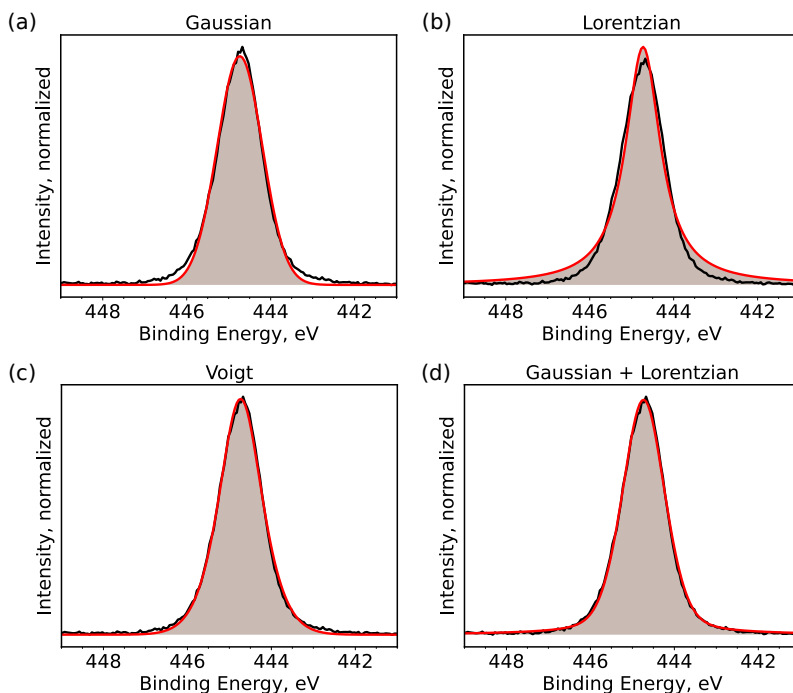
Figure 4.7: Fits of the In 3d$_{5/2}$ core level spectrum of In$_2$O$_3$(111) with four different fit functions to illustrate the effect of peak shapes on the fit: (a) a pure Gaussian function, (b) a pure Lorentzian, (c) a Voigt function and (d) sum of a Gaussian and a Lorentzian function.

To illustrate the effect of peak shape on the fit of an XPS spectrum, Figure 4.7 shows the four fits of the In 3d$_{5/2}$ core level spectrum of In$_2$O$_3$(111) with different fit functions: (a) a pure Gaussian function, (b) a pure Lorentzian, (c) a Voigt function and (d) sum of a Gaussian and a Lorentzian function. The Voigt function and the sum of Gaussian and Lorentzian capture the shape of the core-level quite well. The sum of Gaussian and Lorentzian is slightly more accurate at the tails of the peak and was, therefore, used to fit the In 3d$_{5/2}$ core level spectra in paper [I] and [II].

XPS peaks of metals often show an asymmetric line shape. The asymmetry originates from the metallic band structure that allows the transition of valence electrons across the Fermi level into the conduction band. The energy required for this transition is subtracted from the kinetic energy of the emitted photoelectron, creating an asymmetric tail of the XPS peak. A Doniach-Sunjic lineshape is commonly used to account for the asymmetric shape of metallic peaks [86].

While XPS generally offers extensive information about the electronic structure of various materials, its application becomes challenging when characterizing insulating samples like the Al$_2$O$_3$-supported catalysts studied in this thesis. When an X-ray beam is used to ex-
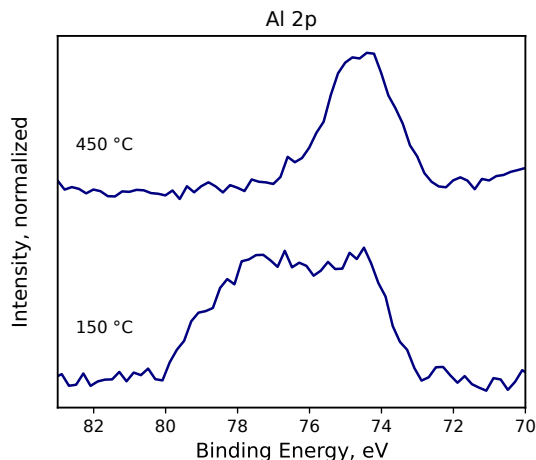
Figure 4.8: Al 2p spectra of a NiMo/Al$_2$O$_3$ catalyst in 0.5 mbar H$_2$ at two different temperatures to illustrate the effect of charging at low temperature on the XPS spectra.

cite electrons from an insulator, the electrons can not be replenished as quickly as they are emitted due to the slow charge transfer within the insulator. As a consequence of that, insulating samples begin to charge positively under X-ray illumination [87]. This charging effect increases the energy needed to excite more photoelectrons and can be observed as a shift to lower kinetic or higher binding energies in the XPS spectrum. For highly insulating samples the charging can reach several hundreds of electron volts. It is possible to calibrate XPS spectrum to account for small shifts due to charging, but significant or inhomogeneous charging make it impossible to obtain usable spectra. There are, however, ways to improve the transfer of electrons to the sample in order to reduce the charging during the measurements. Increasing the temperature of the sample helps to reduce charging and so does increasing the pressure since the gas can provide additional electrons. In UHV-XPS measurements, a flood gun that shoots electrons at the sample can be used to overcome the charging effects.

The effect of charging on the XPS spectra is illustrated in Figure 4.8. The figure shows Al 2p spectra of a NiMo/Al$_2$O$_3$ catalyst in 0.5 mbar H$_2$ at two different temperatures. The spectrum at elevated temperature shows a single symmetric peak at 74.6 eV and the low temperature spectrum shows a broader signal that appears to consist of multiple features. However, the different features in the low temperature spectrum do not originate from chemical shifts but are caused by in homogeneous charging.
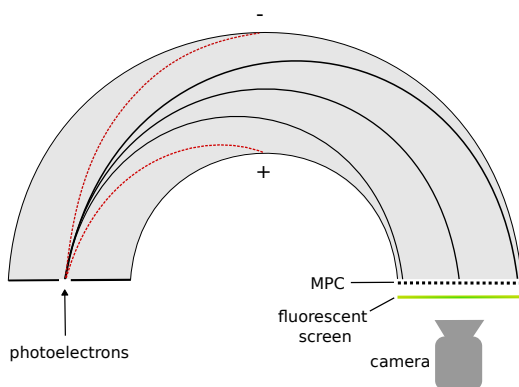
Figure 4.9: Illustration of a hemispherical electron energy analyzer showing the principle of how photoelectrons are separated based on their kinetic energy.

4.2.2 Experimental setup

Above, we discussed that the binding energy of photoelectrons is obtained by measuring their kinetic energy. In this section, we will focus on how the kinetic energy of photoelectrons can be measured in UHV and how an XPS system can be upgraded to allow to measure XPS at elevated pressure.

After emission to vacuum, the photoelectrons are detected using a hemispherical analyzer with two hemispherical plates with opposite charge. As illustrated in Figure 4.9, the charged hemispheres deflect electrons, and the electrons with too high or too low kinetic energy will collide with one of the hemispherical plates. Electrons with a kinetic energy within the chosen pass energy range, are transmitted through the electron analyzer onto the Multi-Channel Plate (MCP), which contains an array of photo multipliers allowing for spatially-resolved multiplication of the electrons onto a fluorescent screen and a CCD camera.

Due to the short IMFP length of electrons in gas, XPS has traditionally been limited to the UHV pressure range. It is, however, possible to extend the pressure range of the technique by modifying the experimental setup. The instrumental challenge is how to design an experimental setup where the sample is kept at an elevated pressure while both the X-ray source and the electron analyzer are under high vacuum, to allow both of these components to function properly.

Figure 4.10 shows how this can be achieved. The X-ray source can be separated from the sample by an X-ray transparent window that allows the X-rays to pass through but effectively blocks gases from the sample environment. Typical materials for these X-ray transparent windows are SiN, SiC or aluminum.

Separating the sample from the electron detector while simultaneously allowing electrons to
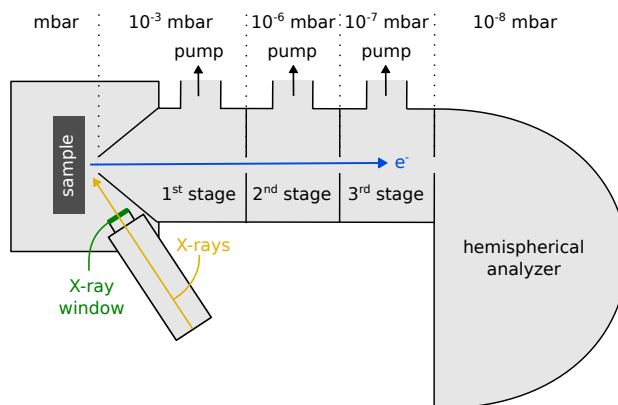
Figure 4.10: Illustration of the setup of an APXPS instrument with an X-ray transparent window to the X-ray source and differential pumping with electrostatic focusing to the electron analyzer. Figure adapted from reference [88].

pass onto the detector is more challenging. The solution is to use a differentially pumped system. A nozzle with a hole is placed a few mm from the sample. The photoelectrons can pass through the hole in the nozzle. The volume behind the nozzle is connected to a pump that lowers the pressure towards the electron analyzer. This reduces the distance that the electrons have to travel through the high pressure region, and reduces the gas transmission into the analyzer. By using multiple differential pumping stages, the pressure in the experimental chamber can be kept in the mbar range, while the electron analyzer is able to operate at the desired pressure of approximately 10^{-8} mbar. To reduce scattering of electrons as they pass through the differential pumping stages towards the hemispherical analyzer, an electron lens system is used to refocus the photoelectron beam [89].

Standard APXPS setups have a nozzle opening with a diameter of approximately 2 mm. Such a nozzle allows measurements at pressures of approximately 10 or 20 mbar. While such pressures are sufficiently high to enable *in situ* and *operando* measurements of a solid sample and the surrounding gas phase, it is still a relatively low pressure by the standards of industrial catalysis.

Instrumental developments have pushed towards closing this pressure gap. Two approaches have been taken to extend the pressure range of APXPS. The first approach is based on development special sample holders that allow to measure AXPXS through graphene-based membranes [90]. The second approach is to optimize the setup for measurements with smaller nozzle openings that allow higher operational pressures in the experimental cell [42]. The POLARIS setup, which enables APXPS measurements at a pressure of several bar, was put into operation a few years ago [42]. These high operating pressures are made possible by the use of hard X-rays in gracing incident angle in combination with micrometer

sized nozzle openings drilled along the X-ray beam profile.

4.3   X-ray Absorption Near Edge Structure

The section above discussed how surfaces can be investigated by studying photoelectrons emitted from the surface after the photoionization by X-rays. In this section we will instead focus on X-ray Absorption Near Edge Structure (XANES) spectroscopy, which is used to probe the electronic structure of unoccupied electronic states.

The X-ray absorption process, used in XANES, is illustrated in Figure 4.11 (a): An incoming X-ray photon of suitable energy excites a core-level electron into an unoccupied electronic state. XANES measures the probability of the absorption of these photons by the sample (absorption cross section) as a function of the photon's energy. When the X-ray photons have sufficient energy to directly excite a core level electron into an unoccupied state, the absorption cross section increases significantly, resulting in an X-ray absorption edge.

XANES spectra of the Mo k-edge for different molybdenum samples are shown in Figure 4.11 (b). The edge position and the post edge features both change with the oxidation state of molybdenum, illustrating how XANES can be used to probe the oxidation state of metals. XANES can be measured in different ways: (i) in transmission mode by measuring the intensity of the X-ray beam before and after passing through the sample; (ii) in fluorescence mode, where the fluorescence due to the relaxation of the excited atom after the X-ray absorption, is measured, assuming that the X-ray absorption is directly proportional to the fluorescence detected; (iii) by measuring the Auger electrons emitted from the excited atom during the relaxation process, assuming that the X-ray absorption is directly proportional to the number of detected electrons. This can be done either by measuring the electrons of a specific Auger process (Auger yield) or by measuring all electrons emitted from the sample (total yield).

In paper [III], we use XANES spectroscopy in transmission mode and fluorescence mode to study the reduction of $NiMo/Al_2O_3$ catalysts by *in situ* measurements of the Ni and Mo k-edge.

Owing to the extended penetration depths of X-rays in matter, XANES exhibits less surface sensitivity than XPS, particularly when employed in fluorescence or transmission mode. Consequently, the differentiation between bulk and surface contributions poses a considerable challenge in XANES measurements.

(a)

(b)

Fermi level

Energy

X-rays

Mo k-edge

Intensity, normalized

MoO$_3$
(Mo^{6+})

MoO$_2$
(Mo^{4+})

Mo
(Mo^{0+})

19950   20000   20050   20100
Photon Energy, eV
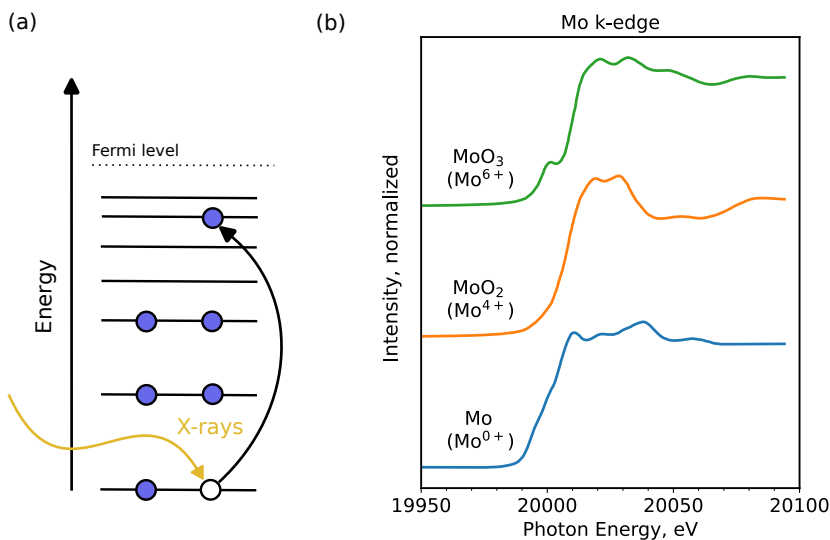
Figure 4.11: Panel (a) illustrates the excitation process of a core-level electron into an unoccupied state which gives rise to the near edge adsorption features probed with XANES. Panel (b) displays XANES spectra of metallic Mo, MoO$_2$ and MoO$_3$, illustrating the sensitivity of the XANES to changes of the metal's oxidation state.

4.4   Diffuse Reflectance Infrared Fourier Transform Spectroscopy

While XPS and XANES study the electronic structure of atoms and molecules, IR-based spectroscopy is used to probe the vibrational states of molecules. Molecular bonds vibrate with discrete frequencies corresponding to specific energies. At a temperature of absolute zero all molecules are in their vibrational ground state and with increasing temperature, higher vibrational states are occupied following Boltzmann's law:

$$\frac{N_i}{N_0} = \frac{g_i}{g_0} e^{-\Delta E/kT}$$

(4.3)

where N_i is the population of the vibrational state i, g_i the degeneracy of state i, ΔE the energy difference between the ground state 0 and state i, k the Boltzmann constant and T the temperature.

Particular vibrational modes of a molecules can be excited by the absorption of a photon of the correct energy. Transitions between the nearest vibrational states typically have transition energies in the medium and far IR region (4000 - 400 cm^{-1} and 400 - 10 cm^{-1}, respectively). The transition between two vibrational modes is subject to selection rules according to which only vibrational modes that are associated with a change in dipole mo-
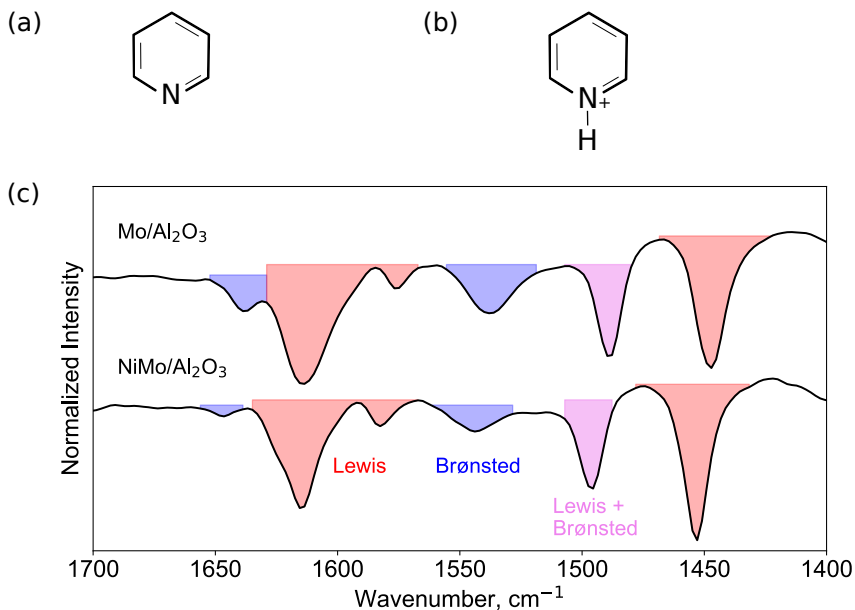
Figure 4.12: Illustration of the structure of (a) a pyridine molecule and (b) a pyridinium ion. Panel (c) shows the DRIFTS spectra of Mo/Al_2O_3 and $NiMo/Al_2O_3$ at 150 $^\circ$C after the adsorption of pyridine. The different vibrational bands of pyridine can be assigned to pyridine adsorbed on Brønsted or Lewis acid sites.

ment can be excited directly [38].

Today most IR spectroscopy is done using a Fourier-Transform InfraRed (FTIR) spectrometer. This type of spectrometers are based on a Michelson interferometer. The polychromatic IR beam is split by a beam splitter and reflected by two mirrors to recombine the two beams. The pathlenght difference of the two beams is periodically varied by moving one of the mirrors back and forth. This periodic variation allows to perform a Fourier transform between the time and frequency space to obtain the IR spectrum.

Over the years different types of IR spectroscopy have been developed. In heterogeneous catalysis research, two main methods have been established. The catalyst can be pressed and the IR beam is sent directly through the pressed sample to measure IR absorption. This method was used in paper [**B**] in the work related to this thesis. Alternatively, the catalyst can be ground to a fine powder and the IR beam is focused on the powder, which diffusely reflects the beam at several powder grains and thus amplifies the absorption signal before the IR beam is focused again. The later technique is called Diffuse Reflectance InfraRed Fourier Transform Spectroscopy (DRIFTS). As part of my PhD, I built a DRIFTS setup with which we are now investigating the nature of acid sites on Al_2O_3 supported catalysts.

Table 4.1: Vibrational frequencies of liquid Pyridine and Pyridinium ions in $C_5H_5NH^+$ (Cl^-) given in cm^{-1} [38].

Notation	Pyridine C_5H_5N	Pyridinium ion $C_5H_5NH^+$ (Cl^-)
8a	1583	1638
8b	1577	1608
19a	1481	1535
19b	1436	1485

DRIFTS can be used to study the acid sites of catalysts. There are two types of acid sites. Lewis acid sites that accept electrons from adsorbates and Brønsted sites that donate protons to the adsorbates. The molecule pyridine has been established as a probing molecule for Lewis and Brønsted acid sites of catalysts. The structure of pyridine is displayed in Figure 4.12 (a). When pyridine is adsorbed on a Lewis acid site, it has a few vibrational bands between 1700 cm^{-1} and 1400 cm^{-1}. If pyridine is adsorbed on a Brønsted site, the pyridine molecule is protonated to a pyridinium ion (see Figure 4.12 (b)). The vibrational bands of pyridinium are shifted from the vibrational bands of pyridine by approximately 50 cm^{-1}, which allows to differentiate the IR spectra of the two molecules quite clearly. Table 4.1 lists the vibrational bands of liquid pyridine and pyridinium ions. The shift of vibrational bands based on the protonation of pyridine allows to use the molecule to probe the Lewis and Brønsted acid sites of a catalyst.

Figure 4.12 (c) shows the DRIFTS spectra of a Mo/Al_2O_3 and a $NiMo/Al_2O_3$ catalyst after pyridine adsorption. These are the same catalysts that were studied in manuscript [III]. The presented spectra were normalized by dividing the spectra by reference spectra taken in vacuum at the same temperature prior to the pyrindine adsorption. The DRIFTS spectra show that the co-impregnation of the Mo/Al_2O_3 with Ni significantly reduces the number of Brønsted acid sites on the catalysts. Additionally, the observed bands shift to a slightly higher wavenumber. This shift to higher wavenumbers shows an increase in the strength of the acid sites [38].

4.5 Transmission Electron Microscopy

In transmission electron microscopy (TEM), an electron beam of approximately 80-300 kV is directed through a sample and an image is detected on the other side of the sample by detecting the electron beam using for example a fluorescent screen. Figure 4.13 (a) shows an illustration of a TEM setup. Throughout the electron microscope different electronic lenses and apertures are used to shape the beam and increase the magnification of the image.

The contrast of the TEM image is created by the interaction of the electrons with the sample. Differences in the inelastic scattering of electrons or diffraction of electrons on

(a) Electron gun

Condenser lenses

Sample

Objective lens

Intermediate lens

Projector lens

Viewing screen

Illumination

Image formation

Projection

Detection

(b) NiMo(1:2)/Al$_2$O$_3$

(c) Al

(d) Ni

(e) Mo
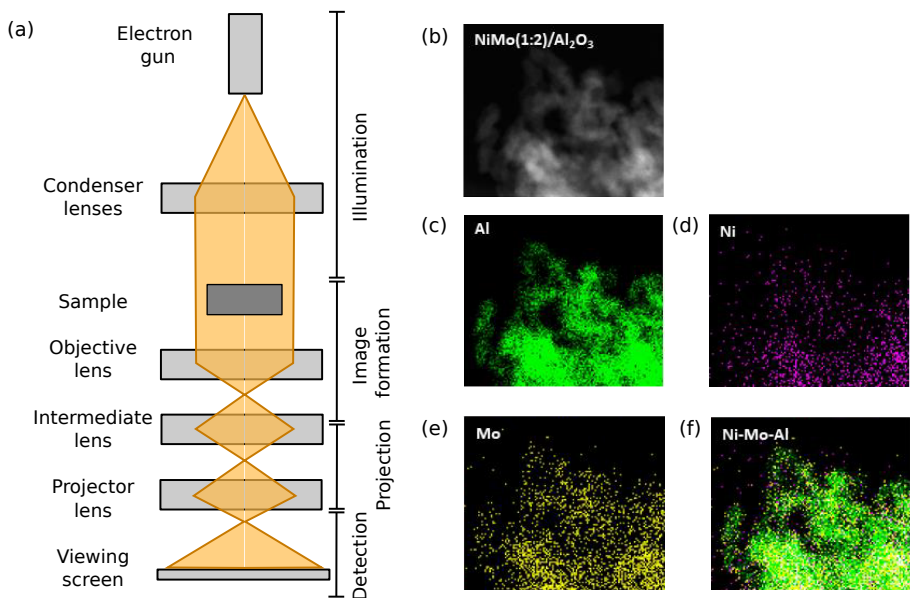
(f) Ni-Mo-Al

Figure 4.13: (a) Illustration of the lens system of a TEM setup. The figure was adapted from references [91, 92]. (b) STEM image of a NiMo/Al$_2$O$_3$ catalyst. (c)-(f) show the EDX images from the STEM image in (b) for Al, Ni, Mo and the overlay the three metals, respectively. Images (b)-(f) were taken from paper [iii].

different spots on the sample give rise to the TEM contrast. Nowadays, TEM microscopes can reach a resolution of up to 0.2 nm [92]. The resolution is limited by the electromagnetic lenses, which suffer from multiple kinds of aberrations.

The TEM images presented in paper [iii] were recorded in scanning transmission electron microscopy (STEM) mode. In this mode, the electron beam is focused on the sample and scanned across the sample to obtain an image. Figure 4.13 (b) shows a STEM image of a NiMo/Al$_2$O$_3$ catalyst showing the irregular structure of the powder catalyst.

In order to assess the uniform impregnation of the Al$_2$O$_3$ support with Ni and Mo, an analysis of the sample composition can be carried out using a TEM microscope. This analysis can be performed using either Electron Energy Loss Spectroscopy (EELS) or Energy-Dispersive X-ray spectroscopy (EDX). In our case, EDX was utilized. EDX relies on the inelastic scattering of electrons by the sample. When an electron is scattered inelastically by an atom, a core electron of the atom can be emitted, leaving the atom in an excited electronic state. To relax the atom again, an electron from an outer shell can fill the core hole. This process can be accompanied by the emission of an X-ray photon in a fluorescence process. The wavelength of these photons is element specific. Thus, an element specific image of the sample can be obtained by scanning the electron beam across the sample, measuring an X-ray fluorescence spectrum and decomposing this spectrum by the element specific

energies. Figure 4.13 (c)-(e) shows the EDX images for Al, Ni and Mo, respectively, of the NiMo/Al_2O_3 catalyst. These three images were overlayed on top of each other in 4.13 (f) to illustrate the homogeneity of the deposition of the Ni and Mo on the Al_2O_3 support. The images shows that the two metals were deposited quite evenly on the support.

4.6   Low Energy Electron Diffraction

Low Energy Electron Diffraction (LEED) is an experimental technique that uses the diffraction pattern of electrons to probe surface structures. Figure 4.14 (a) illustrates the basic setup of a LEED instrument. An electron beam is created by heating a filament and accelerating the emitted electrons onto the sample. The electrons are backscattered from the sample and interfere constructively or destructively, resulting in an interference LEED pattern that is detected by the fluorescent screen. In order to ensure that this fluorescent screen only detects elastically backscattered electrons, the backscattered electrons travel through a few electrical grids that filter out most of the inelastically scattered electrons by applying an electrical potential.

The detected LEED pattern represent the reciprocal lattice of the sample's surface. To only measure the surface structure and reduce contributions from the bulk, LEED uses low energy electrons, which reduces the electron's probing depth (in contrast to TEM). Typical beam energies are around 20 – 1000 eV resulting in a probing depth of approximately 10 Å.

A full analysis of the LEED pattern allows to obtain bond lengths and angles of the surface atoms, by a detailed analysis of the relative intensities of the diffraction spots as a function of the electron energy. In manuscript [I] and [II] LEED was, however, only used to monitor the surface structure of the In_2O_3(111) surfaces. Figure 4.14 (b) shows a LEED image of
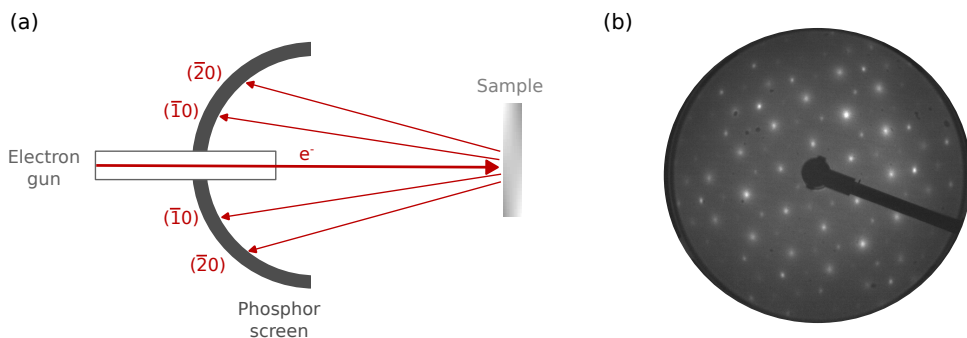
Figure 4.14: (a) Schematic sketch of a LEED setup and (b) a LEED image of an In_2O_3(111) surface taken with an acceleration volatage of 63 eV.

the $In_2O_3(111)$ surface with the 120 ° surface symmetry.

4.7   Temperature Programmed Reduction

Temperature Programmed Reduction (TPR) probes the temperature dependence of the reduction of an oxide catalyst. A reducing gas, such as hydrogen or CO, is continuously passed over the catalyst while the catalyst is slowly heated. The reduction of the catalyst is monitored by measuring the gas composition of the reducing gas before and after passing through the catalyst using a thermal conductivity detector or a mass spectrometer, or an equivalent method.

For the NiMo catalysts, the TPR spectrum profile provides information on how the ratio of different metals affects the reduction behaviour and how the reduction is affected by additional doping. Figure 4.15 shows TRP spectra of Mo/Al_2O_3, Ni/Al_2O_3 and $NiMo/Al_2O_3$ catalysts in H_2 gas as a function of temperature. The Mo/Al_2O_3 catalyst shows a reduction peak at approximately 500 °C and the Ni/Al_2O_3 shows a peak at approximately 550 °C. In the literature the peaks are respectively assigned to the reduction of MoO_3 to MoO_2 and the reduction of NiO to Ni [77]. For the bimetallic $NiMo/Al_2O_3$ catalyst, the first reduction peak is observed at a temperature of approximately 400 °C. This illustrates that the two metals influences each other's reduction behavior. To gain more insight into the reduction mechanism of the bimetallic catalyst, we studied their reduction in more detail with complementary techniques in paper [III]. Additionally, we used TPR and APXPS in paper [v] to investigate how the promotion of $NiMo/Al_2O_3$ catalysts with Pt and Ru
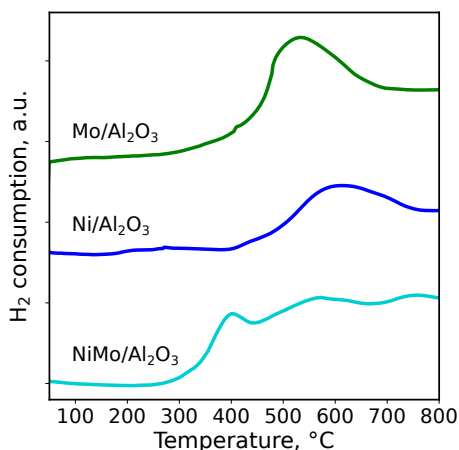
Figure 4.15: H_2 TRP spectra of Mo/Al_2O_3, Ni/Al_2O_3 and $NiMo/Al_2O_3$ as a function of temperature.

influences their reduction in H_2.

4.8 Density Functional Theory

Density Functional Theory (DFT) is a theoretical method used to calculate the electronic structure of atoms, molecules and solids from the fundamental laws of quantum mechanics [93]. To gain a basic understanding of the DFT approach, let us consider a system consisting of M nuclei and N electrons. The state of this system is described by its Hamiltonian operator $\mathcal{H}$, defined as the sum of the kinetic energy operator and the potential energy operator of the system

$$\mathcal{H} = \mathcal{T}_{\text{nucl}} + \mathcal{T}_{\text{el}} + \mathcal{V}_{\text{nucl}-\text{nucl}} + \mathcal{V}_{\text{nucl}-\text{el}} + \mathcal{V}_{\text{el}-\text{el}} \tag{4.4}$$

where $\mathcal{T}_{\text{nucl}}$ is the kinetic energy operator of the nuclei, $\mathcal{T}_{\text{el}}$ the kinetic energy operator of the electrons and the three electrostatic potential operators $\mathcal{V}$ describe the interaction between the electrons and nuclei.

The total energy of such a system in its ground state E is given by the time independent Schrödinger equation:

$$\mathcal{H}\Phi(\mathbf{R}, \mathbf{r}) = E\Phi(\mathbf{R}, \mathbf{r}) \tag{4.5}$$

with $\Phi(\mathbf{R}, \mathbf{r})$ the electronic wavefunction of the system defined by the coordinates of all M nuclei $\mathbf{R}$ and the coordinates of all N electrons $\mathbf{r}$.

In order to solve the Schrödinger equation, the wavefunction $\Phi(\mathbf{R}, \mathbf{r})$ needs to be obtained. However, due to the complexity of the electron-electron interaction $\mathcal{V}_{\text{el}-\text{el}}$, the Schrödinger equation can only be solved analytically for one-electron systems. To overcome this severe limitation, different methods have been developed to solve the Schrödinger equation numerically using approximations where necessary. The first approximation is usually the Born-Oppenheimer-approximation, which treats the wavefunctions of the electrons and nuclei independently of each other. This approach is based on the fact that the nuclei move significantly slower than electrons and can thus be considered stationary relative to the electrons [94].

Traditional electronic structure methods use the Born-Oppenheimer-approximation to approximate solutions to the Schrödinger equation by approximating the wavefunctions of all electrons in the system. In the 60's, Hohenberg and Kohn proposed an alternative approach which forms the foundation of DFT. They provided a formal proof that the ground-state of

a system with N electrons is uniquely defined by an electron density that depends on only three spatial coordinates [95]. This approach forms the foundation of modern DFT and significantly reduces the complexity of the Schrödinger equation, since DFT now only needs to solve the density function $\rho(\mathbf{r})$, instead of solving the wavefunctions as a function of the coordinates of all electrons which sums up to $3 \cdot N$ spatial coordinates. This significantly reduces the calculation time of DFT compared to traditional electronic structure methods. However, this approach neglects the electron-electron interaction $\mathcal{V}_{el-el}$. While Hohenberg and Kohn proved that there is a functional that accounts for this electron-electron interaction, they did not propose how to define this potential.

A year later, Kohn and Sham introduced an effective potential to model the external potentials and approximates the electron exchange and correlation interactions [96]. Since then many different exchange-correlation energy functional have been developed. However, the description of electron exchange and correlation remains the central challenge of DFT. The functionals used for the calculations in this thesis are so-called hybrid functionals which obtain the exchange-correlation energy functional partially from exact Hartree–Fock theory and partially from approximations.

Several software packages have been developed to calculate electronic structures of matter using the DFT approach. The calculations shown in this thesis were done with a software package called VASP (Vienna *Ab-inition* Simulation Package) [97–100]. The calculations were done by my collaborator Dr. Minttu Kauppinen from Chalmers University in Gothenburg, Sweden and University of Jyväskylä, Finland. The computational resources were provided by C3SE (Centre for scientific and technical computing at Chalmers University of Technology in Gothenburg, Sweden) and NSC (National Supercomputer Centre at Linköping University) through a SNIC grant.

Chapter 5

Summary & Outlook

This thesis focuses on the characterization of the fundamental properties of two oxide catalysts. The two investigated oxide catalysts are $In_2O_3(111)$ model catalysts and NiMo-oxide catalysts. The $In_2O_3(111)$ model catalysts are studied as a model system for In_2O_3-based catalysts used for CO_2 hydrogenation to methanol. Manuscript [I] and [II] investigate the interaction of the $In_2O_3(111)$ surface with CO_2, syngas and potential reaction intermediates using photoelectron spectroscopy and complementary DFT calculations. The studies provide insights into the adsorption geometry of the respective molecules on the surface. CO_2 gas adsorbs as a carbonate on the $In_2O_3(111)$ at low pressure and temperature. At elevated pressure and temperature, the adsorption of carboxyl groups was observed on the surface alongside the carbonate. Furthermore, it was observed that CO in the syngas mixture promotes the formation of methoxy-groups on the $In_2O_3(111)$. Additionally, the poising effect of H_2O and H_2S on the CO_2 adsorption on the surface was investigated. The studies show that OH-groups originating from dissociated water on the surface limit the adsorption of CO_2 on the surface, and the dissociative adsorption of H_2S completely blocks the CO_2 adsorption.

For future investigations, more controlled studies on the adsorption and the poisoning effect of H_2S and other sulfur-based contaminations on the $In_2O_3(111)$ surface could provide further insights into the sulfur-based surface poising of this surface. Additional studies on the surface poisoning effect of other syngas contaminants such as NO_x could also be beneficial. Furthermore, the surface science investigations in this thesis focus exclusively on the $In_2O_3(111)$ surface. In order to obtain a more comprehensive picture of the surface reactions on In_2O_3 surfaces, studies on other In_2O_3 surfaces are necessary. In that context, the $In_2O_3(110)$ surface is of special interest, since this surface has also been identified as an active surface for CO_2 hydrogenation. The experiments presented in this thesis are *in situ* and *ex situ* investigations of the $In_2O_3(111)$ surface. While such fundamental invest-

igation of the $In_2O_3(111)$ surface provide a lot of insights into the adsorption of gases on the surface, they may not show the full picture of the surface's behavior under reaction conditions. Therefore, additional experimental studies of the $In_2O_3(111)$ surface under reaction conditions are of high interest to facilitate the understanding of the reaction mechanism. However, the CO_2 hydrogenation reaction to methanol typically requires pressures of 10 bar or even higher. This requirement for high pressure makes it very challenging to study these type of reactions with the electron-based techniques used in this thesis. However, technical development of electron-based spectroscopy might allow for measurements in this pressure range in future. Otherwise, complementary *operado* studies of $In_2O_3(111)$ might be possible by optical techniques such as IR-spectroscopy, Raman spectroscopy or XAS.

The second part of this thesis investigates the reduction of alumina supported NiMo-oxide catalysts and model systems of these catalysts. The experiments show that Ni and Mo facilitate each other's reduction, and highlight the impact of the alumina support and noble metal promotors on the reduction of the catalysts. To gain a more detailed understanding of the reduction process of NiMo-oxide catalysts, we designed a model system of these catalysts based on $NiMoO_4$ nanoparticles and performed *in situ* experiments on these model catalysts. The experiments indicate that the reduction of the $NiMoO_4$ nanoparticles proceeds through a phase separation of the Ni- and Mo-oxide.

For future investigations of the NiMo-oxide catalysts, it would be beneficial to optimizing the deposition process of the nanoparticles to ensure that the resulting particles show more resemblance with the industrial catalyst. Increasing the resemblance of the $NiMoO_4$ nanoparticle model catalyst to the industrial catalysts involves decreasing the size of the nanoparticles, optimizing the respective metal ratio, depositing the nanoparticles on alumina substrate and try to grow trimetalic catalysts to model the effect of the noble metal promotors. The experiments on the NiMo-oxide catalysts that are presented in this thesis were limited to the reduction of NiMo-oxide catalysts and model systems of these catalysts. Additional *in situ* and *operando* studies on the interaction of the NiMo-oxide catalysts with organic molecules will provide more insight into the application of these catalysts for biofuel upgrading.

References

1. Chorkendorff, I. and Niemantsverdriet, J.W. **Concepts of modern catalysis and kinetics, 2nd edn** (Wiley-VCH, Weinheim, 2007).

2. Wisniak, J. **The History of Catalysis. From the Beginning to Nobel Prizes**. *Educacion Quimica* **21,** 60–69 (2010).

3. Berzelius, J. **Quelques Idées sur une Nouvelle Force Agissant Dans les Combinaisons des Corps Organiques**. *Ann. Chim.* **61,** 146–151 (1836).

4. Ertl, G. **Reactions at surfaces: from atoms to complexity** (Nobel Lecture, 2007).

5. Kittel, C. **Introduction to Solid State Physics** 8th ed. (Wiley, 2004).

6. De Gregorio, G. L., Burdyny, T., Loiudice, A., Iyengar, P., Smith, W. A. & Buonsanti, R. **Facet-Dependent Selectivity of Cu Catalysts in Electrochemical CO_2 Reduction at Commercially Viable Current Densities**. *ACS Catalysis* **10,** 4854–4862 (2020).

7. Somorjai, G. A. & Li, Y. **Introduction to Surface Chemistry and Catalysis** 2nd ed. (Wiley, 1994).

8. Somorjai, G. A. **On the mechanism of sulfur poisoning of platinum catalysts**. *Journal of Catalysis* **27,** 453–456 (1972).

9. Bartholomew, C. H. **Mechanisms of nickel catalyst poisoning. C,** 81–104 (Elsevier Science Publishers B.V., 1987).

10. Khan, H., Sarkar, S., Pal, M., Bera, S. & Jana, S. *Indium Oxide Based Nanomaterials: Fabrication Strategies, Properties, Applications, Challenges and Future Prospect* doi:10.5772/intechopen.94743. IntechOpen. 2020.

11. Pussi, K., Matilainen, A., Dhanak, V. R., Walsh, A., Egdell, R. G. & Zhang, K. H. **Surface structure of In_2O_3(111) (1 x 1) determined by density functional theory calculations and low energy electron diffraction**. *Surface Science* **606,** 1–6 (2012).

12. Morales, E. H., He, Y., Vinnichenko, M., Delley, B. & Diebold, U. **Surface structure of Sn-doped In_2O_3(111) thin films by STM**. *New Journal of Physics* **10,** 0–11 (2008).

13. Henrich, V. E. & Cox, P. A. **The Surface Science of Metal Oxides** 1st ed. (Cambridge University Press, 1994).

14. Wagner, M., Seiler, S., Meyer, B., Boatner, L. A. & Schmid, M. **Reducing the In_2O_3(111) Surface Results in Ordered Indium Adatoms. 3,** 1–6 (2014).

15. Frei, M. S., Capdevila-Cortada, M., García-Muelas, R., Mondelli, C., López, N., Stewart, J. A., Curulla Ferré, D. & Pérez-Ramírez, J. **Mechanism and microkinetics of methanol synthesis via CO_2 hydrogenation on indium oxide**. *Journal of Catalysis* **361,** 313–321 (2018).

16. Braun, D., Scherer, V., Janowitz, C., Galazka, Z., Fornari, R. & Manzke, R. **In-gap states of In$_2$O$_3$ single crystals investigated by scanning tunneling spectroscopy.** *Physica Status Solidi (A) Applications and Materials Science* **211,** 59–65 (2014).

17. Galazka, Z., Uecker, R., Irmscher, K., Schulz, D., Klimm, D., Albrecht, M., Pietsch, M., Ganschow, S., Kwasniewski, A. & Fornari, R. **Melt growth, characterization and properties of bulk In$_2$O$_3$ single crystals.** *Journal of Crystal Growth* **362,** 349–352 (2013).

18. Ohta, H., Orita, M., Hirano, M. & Hosono, H. **Surface morphology and crystal quality of low resistive indium tin oxide grown on yittria-stabilized zirconia.** *Journal of Applied Physics* **91,** 3547–3550 (2002).

19. Koida, T. & Kondo, M. **High electron mobility of indium oxide grown on yttria-stabilized zirconia.** *Journal of Applied Physics* **99** (2006).

20. Zhang, K. H., Lazarov, V. K., Lai, H. H. & Egdell, R. G. **Influence of temperature on the epitaxial growth of In$_2$O$_3$ thin films on Y-ZrO$_2$(111).** *Journal of Crystal Growth* **318,** 345–350 (2011).

21. Franceschi, G., Wagner, M., Hofinger, J., Krajňák, T., Schmid, M., Diebold, U. & Riva, M. **Growth of In$_2$O$_3$(111) thin films with optimized surfaces.** *Physical Review Materials* **3,** 1–10 (2019).

22. Jain, A., Ong, S. P., Hautier, G., Chen, W., Richards, W. D., Dacek, S., Cholia, S., Gunter, D., Skinner, D., Ceder, G. & Persson, K. A. **Commentary: The materials project: A materials genome approach to accelerating materials innovation.** *APL Materials* **1** (2013).

23. *The Materials Project* `https://next-gen.materialsproject.org/` [Accessed: (October 2023)].

24. Davey, W. P. **Precision measurements of the lattice constants of twelve common metals.** *Physical Review* **25,** 753–761 (1925).

25. Cheetham, A. K. & Hope, D. A. O. **Magnetic ordering and exchange effects in the antiferromagnetic solid solutions.** *Physical Review B* **27,** 6964–6967 (1983).

26. Dey, S., Bhattacharjee, S., Chaudhuri, M. G., Bose, R. S., Halder, S. & Ghosh, C. K. **Synthesis of pure nickel(III) oxide nanoparticles at room temperature for Cr(VI) ion removal.** *RSC Advances* **5,** 54717–54726 (2015).

27. De Castro, I. A., Datta, R. S., Ou, J. Z., Castellanos-Gomez, A., Sriram, S., Daeneke, T. & Kalantar-zadeh, K. **Molybdenum Oxides – From Fundamentals to Functionality.** *Advanced Materials* **29,** 1–31 (2017).

28. Magnéli, A., Andersson, G., Sundkvist, G. & Sundkvist, G. **On the MoO$_2$ Structure Type. 9,** 1378–1381 (1955).

29. Carcia, P. F. & McCarron, E. M. **Synthesis and properties of thin film polymorphs of molybdenum trioxide**. *Thin Solid Films* **155,** 53–63 (1987).

30. Chithambararaj, A. & Bose, A. C. **Hydrothermal synthesis of hexagonal and orthorhombic MoO$_3$ nanoparticles**. *Journal of Alloys and Compounds* **509,** 8105–8110 (2011).

31. Yang, L., Wang, J., Wan, Y., Li, Y., Xie, H., Cheng, H. & Seo, H. J. **Structure and effective visible-light-driven photocatalytic activity of α-NiMoO$_4$ for degradation of methylene blue dye**. *Journal of Alloys and Compounds* **664,** 756–763 (2016).

32. Rodriguez, J. A., Chaturvedi, S., Hanson, J. C., Albornoz, A. & Brito, J. L. **Electronic properties and phase transformations in CoMoO$_4$ and NiMoO$_4$: XANES and time-resolved synchrotron XRD studies**. *Journal of Physical Chemistry B* **102,** 1347–1355 (1998).

33. Di Renzo, F., Mazzocchia, C., Thomas, G. & Vernay, A. M. **Formation and properties of the solid solution of NiO in NiMoO$_4$**. *Reactivity of Solids* **6,** 145–155 (1988).

34. Mazzocchia, C., Aboumrad, C., Diagne, C., Tempesti, E., Herrmann, J. M. & Thomas, G. **On the NiMoO$_4$ oxidative dehydrogenation of propane to propene: some physical correlations with the catalytic activity**. *Catalysis Letters* **10,** 181–191 (1991).

35. Christmann, K. **Introduction to Surface Physical Chemistry** (Springer, 2013).

36. Over, H., Kim, Y. D., Seitsonen, A. P., Wendt, S., Lundgren, E., Schmid, M., Varga, P., Morgante, A. & Ertl, G. **Atomic-scale structure and catalytic reactivity of the RuO$_2$(110) surface**. *Science* **287,** 1474–1476 (2000).

37. Weaver, J. F. **Surface chemistry of late transition metal oxides**. *Chemical Reviews* **113,** 4164–4215 (2013).

38. Wachs, I. & Bañares, M. **Springer Handbook of Advanced Catalyst Characterization** (Springer International Publishing, 2023).

39. Suchorski, Y. & Rupprechter, G. **Heterogeneous Surfaces as Structure and Particle Size Libraries of Model Catalysts**. *Catalysis Letters* **148,** 2947–2956 (2018).

40. Barroo, C., Wang, Z. J., Schlögl, R. & Willinger, M. G. **Imaging the dynamics of catalysed surface reactions by in situ scanning electron microscopy**. *Nature Catalysis* **3,** 30–39 (2020).

41. Garcia-Martinez, F., García-Fernández, C., Simonovis, J. P., Hunt, A., Walter, A., Waluyo, I., Bertram, F., Merte, L. R., Shipilin, M., Pfaff, S., Blomberg, S., Zetterberg, J., Gustafson, J., Lundgren, E., Sánchez-Portal, D., Schiller, F. & Ortega, J. E. **Catalytic Oxidation of CO on a Curved Pt(111) Surface: Simultaneous Ignition at All Facets through a Transient CO-O Complex****. *Angewandte Chemie - International Edition* **59,** 20037–20043 (2020).

42. Amann, P., Degerman, D., Lee, M. T., Alexander, J. D., Shipilin, M., Wang, H. Y., Cavalca, F. *et al.* **A high-pressure x-ray photoelectron spectroscopy instrument for studies of industrially relevant catalytic reactions at pressures of several bars.** *Review of Scientific Instruments* **90** (2019).

43. Salmeron, M. & Eren, B. **High-Pressure Scanning Tunneling Microscopy.** *Chemical Reviews* **121,** 962–1006 (2021).

44. Shepherd, G. **Methanol. 1,** 54–56 (2005).

45. Malik, M. I., Abatzoglou, N. & Achouri, I. E. **Methanol to Formaldehyde: An Overview of Surface Studies and Performance of an Iron Molybdate Catalyst.** *Catalysts* **11** (2021).

46. Ye, R. P., Ding, J., Gong, W., Argyle, M. D., Zhong, Q., Wang, Y., Russell, C. K., Xu, Z., Russell, A. G., Li, Q., Fan, M. & Yao, Y. G. **CO_2 hydrogenation to high-value products via heterogeneous catalysis.** *Nature Communications* **10** (2019).

47. Kunkes, E. L., Studt, F., Abild-Pedersen, F., Schlögl, R. & Behrens, M. **Hydrogenation of CO_2 to methanol and CO on $Cu/ZnO/Al_2O_3$: Is there a common intermediate or not? This work is dedicated to the memory and achievements of Dr. Haldor Topsøe.** *Journal of Catalysis* **328,** 43–48 (2015).

48. Topsøe, N. Y. & Topsøe, H. **On the nature of surface structural changes in Cu/ZnO methanol synthesis catalysts.** *Topics in Catalysis* **8,** 267–270 (1999).

49. Martin, O., Martín, A. J., Mondelli, C., Mitchell, S., Segawa, T. F., Hauert, R., Drouilly, C., Curulla-Ferré, D. & Pérez-Ramírez, J. **Indium oxide as a superior catalyst for methanol synthesis by CO_2 hydrogenation.** *Angewandte Chemie - International Edition* **55,** 6261–6265 (2016).

50. Sun, K., Fan, Z., Ye, J., Yan, J., Ge, Q., Li, Y., He, W., Yang, W. & Liu, C. J. **Hydrogenation of CO_2 to methanol over In_2O_3 catalyst.** *Journal of CO2 Utilization* **12,** 1–6 (2015).

51. Zhu, S., Scardamaglia, M., Kundsen, J., Sankari, R., Tarawneh, H., Temperton, R., Pickworth, L. *et al.* **HIPPIE: A new platform for ambient-pressure X-ray photoelectron spectroscopy at the MAX IV Laboratory.** *Journal of Synchrotron Radiation* **28,** 624–636 (2021).

52. Zhang, X., Kirilin, A. V., Rozeveld, S., Kang, J. H., Pollefeyt, G., Yancey, D. F., Chojecki, A., Vanchura, B. & Blum, M. **Support Effect and Surface Reconstruction in In_2O_3/ m-ZrO_2 Catalyzed CO_2 Hydrogenation.** *ACS Catalysis* **12,** 3868–3880 (2022).

53. Frei, M. S., Mondelli, C., García-Muelas, R., Kley, K. S., Puértolas, B., López, N., Safonova, O. V., Stewart, J. A., Curulla Ferré, D. & Pérez-Ramírez, J. **Atomic-scale engineering of indium oxide promotion by palladium for methanol production via CO_2 hydrogenation.** *Nature Communications* **10,** 1–11 (2019).

54. Araújo, T. P., Morales-Vidal, J., Giannakakis, G., Mondelli, C., Eliasson, H., Erni, R., Stewart, J. A., Mitchell, S., López, N. & Pérez-Ramírez, J. **Reaction-Induced Metal-Metal Oxide Interactions in Pd-In$_2$O$_3$/ZrO$_2$ Catalysts Drive Selective and Stable CO$_2$ Hydrogenation to Methanol**. *Angewandte Chemie - International Edition* **202306563** (2023).

55. Posada-Borbón, A. & Grönbeck, H. **CO$_2$ adsorption on hydroxylated In$_2$O$_3$(110)**. *Physical Chemistry Chemical Physics* **21,** 21698–21708 (2019).

56. Posada-Borbón, A. & Grönbeck, H. **Hydrogen adsorption on In$_2$O$_3$(111) and In$_2$O$_3$(110)**. *Physical Chemistry Chemical Physics* **22,** 16193–16202 (2020).

57. Posada-Borbón, A. & Grönbeck, H. **A First-Principles-Based Microkinetic Study of CO$_2$ Reduction to CH$_3$OH over In$_2$O$_3$(110)**. *ACS Catalysis* **11,** 9996–10006 (2021).

58. Zhou, Z., Qin, B., Li, S. & Sun, Y. **A DFT-based microkinetic study on methanol synthesis from CO$_2$ hydrogenation over the In$_2$O$_3$ catalyst**. *Physical Chemistry Chemical Physics* **23,** 1888–1895 (2021).

59. Li, K., Wei, Z., Chang, Q. & Li, S. **DFT-based microkinetic studies on methanol synthesis from CO$_2$ hydrogenation over In$_2$O$_3$ and Zr-In$_2$O$_3$ catalysts**. *Physical Chemistry Chemical Physics* **25,** 14961–14968 (2023).

60. Wang, H., Male, J. & Wang, Y. **Recent advances in hydrotreating of pyrolysis bio-oil and its oxygen-containing model compounds**. *ACS Catalysis* **3,** 1047–1070 (2013).

61. Aryee, E., Dalai, A. K. & Adjaye, J. **Synthesis and Characterization of NiMo Catalysts Supported on Fine Carbon Particles for Hydrotreating: Effects of Metal Loadings in Catalyst Formulation**. *Frontiers in Chemical Engineering* **3,** 1–14 (2021).

62. Mortensen, P. M., Grunwaldt, J. D., Jensen, P. A., Knudsen, K. G. & Jensen, A. D. **A review of catalytic upgrading of bio-oil to engine fuels**. *Applied Catalysis A: General* **407,** 1–19 (2011).

63. Zakzeski, J., Bruijnincx, P. C., Jongerius, A. L. & Weckhuysen, B. M. **The catalytic valorization of lignin for the production of renewable chemicals**. *Chemical Reviews* **110,** 3552–3599 (2010).

64. Thallada, B., Kumar, A., Jindal, M. & Maharana, S. **Lignin biorefinery: New horizons in catalytic hydrodeoxygenation for the production of chemicals**. *Energy and Fuels* **35,** 16965–16994 (2021).

65. Cheng, F. & Brewer, C. E. **Producing jet fuel from biomass lignin: Potential pathways to alkyl-benzenes and cycloalkanes**. *Renewable and Sustainable Energy Reviews* **72,** 673–722 (2017).

66. Sharifzadeh, M., Sadeqzadeh, M., Guo, M., Borhani, T. N., Murthy Konda, N. V., Garcia, M. C., Wang, L., Hallett, J. & Shah, N. **The multi-scale challenges of biomass fast pyrolysis and bio-oil upgrading: Review of the state of art and future research directions**. *Progress in Energy and Combustion Science* **71,** 1–80 (2019).

67. Murugappan, K., Anderson, E. M., Teschner, D., Jones, T. E., Skorupska, K. & Román-Leshkov, Y. **Operando NAP-XPS unveils differences in MoO_3 and Mo_2C during hydrodeoxygenation**. *Nature Catalysis* **1,** 960–967 (2018).

68. Koklyukhin, A. S., Mozhaev, A. V., Sal'nikov, V. A. & Nikul'shin, P. A. **Promoter nature effect on the sensitivity of $Ni–Mo/Al_2O_3$, $Co–Mo/Al_2O_3$, and $Ni–Co–Mo/Al_2O_3$ catalysts to dodecanoic acid in the co-hydrotreating of dibenzothiophene and naphthalene**. *Kinetics and Catalysis* **58,** 463–470 (2017).

69. Topsøe, H., Clausen, B. S., Topsøe, N. Y. & Zeuthen, P. **Progress in the Design of Hydrotreating Catalysts Based on Fundamental Molecular Insight**. *Studies in Surface Science and Catalysis* **53,** 77–102 (1989).

70. Helveg, S., Lauritsen, J. V., Lægsgaard, E., Stensgaard, I., Nørskov, J. K., Clausen, B. S., Topsøe, H. & Besenbacher, F. **Atomic-scale structure of single-layer MoS_2 nanoclusters**. *Physical Review Letters* **84,** 951–954 (2000).

71. Hansen, L. P., Ramasse, Q. M., Kisielowski, C., Brorson, M., Johnson, E., Topsøe, H. & Helveg, S. **Atomic-scale edge structures on industrial-style MoS_2 nanocatalysts**. *Angewandte Chemie - International Edition* **50,** 10153–10156 (2011).

72. Bruix, A., Füchtbauer, H. G., Tuxen, A. K., Walton, A. S., Andersen, M., Porsgaard, S., Besenbacher, F., Hammer, B. & Lauritsen, J. V. **In Situ Detection of Active Edge Sites in Single-Layer MoS_2 Catalysts**. *ACS Nano* **9,** 9322–9330 (2015).

73. Mom, R. V., Louwen, J. N., Frenken, J. W. & Groot, I. M. **In situ observations of an active MoS_2 model hydrodesulfurization catalyst**. *Nature Communications* **10,** 1–8 (2019).

74. Laine, J. & Pratt, K. C. **Hydrodesulfurization activity and transformations of nickel molybdate hydrate**. *Reaction Kinetics and Catalysis Letters* **10,** 207–211 (1979).

75. Nag, N. K., Fraenkel, D., Moulijn, J. A. & Gates, B. C. **Characterization of hydroprocessing catalysts by resolved temperature-programmed desorption, reduction and sulfiding**. *Journal of Catalysis* **66,** 162–170 (1980).

76. Wang, Y., Xiong, G., Liu, X., Yu, X., Liu, L., Wang, J., Feng, Z. & Li, C. **Structure and reducibility of $NiO-MoO_3/\gamma-Al_2O_3$ catalysts: Effects of loading and molar ratio**. *Journal of Physical Chemistry C* **112,** 17265–17271 (2008).

77. Brito, J. L. & Laine, J. **Reducibility of $Ni-Mo/Al_2O_3$-catalysts: A TPR Study**. *Journal of Catalysis* **139,** 540–550 (1993).

78. Blomberg, S., Johansson, N., Kokkonen, E., Rissler, J., Kollberg, L., Preger, C., Franzén, S. M., Messing, M. E. & Hulteberg, C. **Bimetallic nanoparticles as a model system for an industrial NiMo catalyst**. *Materials* **12** (2019).

79. Fu, J., Lym, J., Zheng, W., Alexopoulos, K., Mironenko, A. V., Li, N., Boscoboinik, J. A., Su, D., Weber, R. T. & Vlachos, D. G. **C–O bond activation using ultralow loading of noble metal catalysts on moderately reducible oxides**. *Nature Catalysis* **3**, 446–453 (2020).

80. Albarracin-Suazo, S., Freitas De Lima E Freitas, L., Macqueen, B., Heyden, A., Lauterbach, J. A., Nikolla, E. & Pagán-Torres, Y. J. **Supported Bifunctional Molybdenum Oxide-Palladium Catalysts for Selective Hydrodeoxygenation of Biomass-Derived Polyols and 1,4-Anhydroerythritol**. *ACS Sustainable Chemistry and Engineering* (2021).

81. Hwu, Y. & Margaritondo, G. **Synchrotron radiation and X-ray free-electron lasers (X-FELs) explained to all users, active and potential**. *Journal of Synchrotron Radiation* **28**, 1014–1029 (2021).

82. Boix La Cruz, V. D. **Graphene: Applications in Surface Science Studies** (PhD Thesis, Lund University, 2022).

83. Tanuma, S. & Powell, C. J. **Electron Inelastic Mean Free Paths - Data for 14 organic-compunds over the 50-2000 eV range**. *Surface and Interface Analysis* **21**, 165–176 (1994).

84. Proctor, A. & Sherwood, P. M. A. **Data analysis techniques in X-ray photoelectron spectroscopy**. *Analytical Chemistry* **54**, 13–19 (1982).

85. Tougaard, S. **Practical algorithm for background subtraction**. *Surface Science* **216**, 343–360 (1989).

86. Doniach, S. & Sunjic, M. **Many-electron singularity in X-ray photoemission and X-ray line spectra from metals**. *Journal of Physics C: Solid State Physics* **3**, 285–291 (1970).

87. Merte, L. R., Gustafson, J., Shipilin, M., Zhang, C. & Lundgren, E. **Redox behavior of iron at the surface of an $Fe_{0.01}Mg_{0.99}O(100)$ single crystal studied by ambient-pressure photoelectron spectroscopy**. *Catalysis, Structure and Reactivity* **3**, 95–103 (2017).

88. Karslioglu, O., Nemšák, S., Zegkinoglou, I., Shavorskiy, A., Hartl, M., Salmassi, F., Gullikson, E. M., Ng, M. L., Rameshan, C., Rude, B., Bianculli, D., Cordones, A. A., Axnanda, S., Crumlin, E. J., Ross, P. N., Schneider, C. M., Hussain, Z., Liu, Z., Fadley, C. S. & Bluhm, H. **Aqueous solution/metal interfaces investigated in operando by photoelectron spectroscopy**. *Faraday Discussions* **180**, 35–53 (2015).

89. Starr, D. E., Liu, Z., Hävecker, M., Knop-Gericke, A. & Bluhm, H. **Investigation of solid/vapor interfaces using ambient pressure X-ray photoelectron spectroscopy.** *Chemical Society Reviews* **42,** 5833 (2013).

90. Velasco-Vélez, J. J., Pfeifer, V., Hävecker, M., Wang, R., Centeno, A., Zurutuza, A., Algara-Siller, G., Stotz, E., Skorupska, K., Teschner, D., Kube, P., Braeuninger-Weimer, P., Hofmann, S., Schlögl, R. & Knop-Gericke, A. **Atmospheric pressure X-ray photoelectron spectroscopy apparatus: Bridging the pressure gap**. *Review of Scientific Instruments* **87** (2016).

91. Robin, Sjökvist. **In-situ Study of the Growth, Composition and Morphology of III-V Semiconductor Nanowires** (PhD Thesis, Lund University, 2023).

92. Carter, C. Barry and Williams, David B. **Transmission Electron Microscopy - Diffraction, Imaging, and Spectrometry, 3rd edition** (Springer, 2016).

93. Kurth, S., Marques, M. & Gross, E. in *Encyclopedia of Condensed Matter Physics* (eds Bassani, F., Liedl, G. L. & Wyder, P.) 395–402 (Elsevier, Oxford, 2005).

94. Groß, A. **Theoretical Surface Science: A Microscopic Perspective** (Springer Berlin Heidelberg, 2009).

95. Hohenberg, P. & Kohn, W. **Inhomogeneous Electron Gas**. *Phys. Rev.* **136,** B864–B871 (1964).

96. Kohn, W. & Sham, L. J. **Self-Consistent Equations Including Exchange and Correlation Effects**. *Phys. Rev.* **140,** A1133–A1138 (1965).

97. Kresse, G. & Hafner, J. **Ab initio molecular dynamics for liquid metals**. *Phys. Rev. B* **47,** 558–561 (1993).

98. Kresse, G. & Hafner, J. **Ab initio molecular-dynamics simulation of the liquid-metalamorphous- semiconductor transition in germanium**. *Phys. Rev. B* **49,** 14251–14269 (1994).

99. Kresse, G. & Furthmüller, J. **Efficient iterative schemes for ab initio total-energy calculations using a plane-wave basis set**. *Phys. Rev. B* **54,** 169 (1996).

100. Kresse, G. & Furthmüller, J. **Efficiency of ab-initio total energy calculations for metals and semiconductors using a plane-wave basis set**. *Comput. Mater. Sci.* **6,** 15–50 (1996).

Chapter 6

Summary of Publications and Author Contributions

Paper I: Effect of Different In$_2$O$_3$(111) Surface Terminations on CO$_2$ Adsorption

Gericke, S. M., Kauppinen, M. M., Wagner, M., Riva, M., Franceschi, G., Posada-Borbón, A., Rämisch, L., Pfaff, S., Rheinfrank, E., Imre, A. M., Preobrajenski, A. B., Appelfeller, S., Blomberg, S., Merte, L. R., Zetterberg, J., Diebold, U., Grönbeck, H. & Lundgren, E.

In this paper, we studied the adsorption of CO$_2$ on three different surface terminations of In$_2$O$_3$(111) in a combined XPS and DFT study. We could identify how CO$_2$ adsorbs on the different surface terminations and how hydroxyl groups on the surface limit the adsorption of CO$_2$. Additionally, the adsorption of methanol and formic acid on the In$_2$O$_3$(111) surface were investigated.

I wrote the beamtime proposals and was the main responsible for planning, preparing and leading the XPS experiments. I analyzed the XPS data and discussed the experimental results with Minttu Kauppinen who performed the DFT calculations and wrote the theoretical sections of the manuscript. I wrote the rest of the manuscript.

Paper II: Interaction of In$_2$O$_3$(111) with syngas and the effect of sulfur contaminant on CO$_2$ adsorption on In$_2$O$_3$(111)

Gericke, S. M., Kauppinen, M. M., Wagner, M., Riva, M., Franceschi, G., Rämisch, L., Pfaff, S., Ryan, P., Rheinfrank, E., Imre, A. M., Blomberg, S., Scardamaglia, M., Wang, W., Zetterberg, J., Diebold, U., Grönbeck, H. & Lundgren, E.

In this paper, we present *in situ* APXPS measurements of the interaction of In$_2$O$_3$(111) with CO$_2$, H$_2$ and CO. The measurements are supported by complementary DFT calculations.

Carboxyl-groups were detected on the surface at elevated CO_2 pressure and temperature, and CO appears to promote the formation of methoxy groups on the surface. Additionally, we investigated the poisoning effect of sulfur-based contamination on the surface.

I wrote the beamtime proposals and was the main responsible for planning, preparing and leading the experiments. I analyzed the XPS spectra. Minttu Kauppinen performed the DFT calculations. I wrote the manuscript.

Paper III: In Situ H_2 Reduction of Al_2O_3-Supported Ni- and Mo-Based Catalysts

Gericke, S. M., Rissler, J., Bermeo, M., Wallander, H., Karlsson, H., Kollberg, L., Scardamaglia, M., Temperton, R., Zhu, S., Sigfridsson Clauss, K. G., Hulteberg, C., Shavorskiy, A., Merte, L. R., Messing, M. E., Zetterberg, J. & Blomberg, S.

This paper discusses the reduction of $NiMo/Al_2O_3$ catalysts and model systems of these catalysts in H_2, which was studied *in situ* using APXPS and XANES. Additionally, the morphology of the catalysts was studied with TEM. The *in situ* reduction experiments showed that the reduction is strongly influenced by the Al_2O_3-support as well as the ratio of Ni and Mo.

I took part in the beamtime planning and the beamtime. I analyzed the APXPS data and discussed my results with the other co-authors who analyzed the XANES and TEM data. I wrote the main part of the manuscript.

Paper IV: In situ AP-XPS reduction study of engineered $NiMoO_4$ nanoparticles

Elmroth Nordlander, J., Gericke, S. M., Bermeo Vargas, M., Ternero, P., Wahlqvist, D., Hallböök, F., Scardamaglia, M., Zetterberg, J., Ek, M., Messing, M. & Blomberg, S.

This paper discusses the reduction of $NiMoO_4$ nanoparticles in H_2. The nanoparticles were imaged with TEM before and after the reduction and the reduction was followed *in situ* using APXPS. Our results indicate that the reduction of $NiMoO_4$ nanoparticles proceeds via a phase separation of Ni and Mo.

I took part in the planning and preparation of the beamtime and the measurements. I participated in discussions on the data analysis and the manuscript.
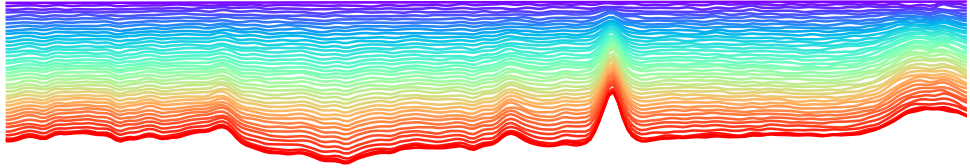
Paper V: In situ APXPS and TPR reduction study of Pd-NiMo and Ru-NiMo catalysts

Hallböök, F., Gericke, S. M., Kristensen, T., Elmroth Nordlander, J., Karagoz, B., Van Spronsen, M., Hulteberg, C., Zetterberg, J. & Blomberg, S.

This paper discusses the reduction of noble metal promoted $NiMo/Al_2O_3$ catalysts in H_2. Our *in situ* APXPS and H_2-TPR study shows that the addition of these noble metals im-

pacts the reduction characteristics of the NiMo-based catalysts. Different reduction behaviors were observed for the promotion with Pd and Ru.

I wrote the beamtime proposal for the APXPS measurements. I took part in the planning and preparation of the beamtime and the measurements. I participated in discussions on the data analysis and the manuscript.

Faculty of Engineering
Department of Physics

LUND

UNIVERSITY